universität wien

MASTERARBEIT / MASTER'S THESIS

Titel der Masterarbeit / Title of the Master's Thesis

„Measuring the time evolution of the particle size distribution of the Vienna Urban aerosol, by combining two parallel differential mobility particle sizers to cover the size range between 3 and 900 nm."

verfasst von / submitted by

Sascia Kästenbauer, BSc

angestrebter akademischer Grad / in partial fulfilment of the requirements for the degree of

Master of Science (MSc)

Wien, 2021 / Vienna, 2021

Studienkennzahl lt. Studienblatt / degree programme code as it appears on the student record sheet:	UA 066 876
Studienrichtung lt. Studienblatt / degree programme as it appears on the student record sheet:	Masterstudium Physik
Betreut von / Supervisor:	Assoz. Prof. Dr. Paul Winkler, Privatdoz.

Abstract

Aerosols are around us and can affect our personal lives in different ways. First of all, it is well known that aerosols have a massive impact on our climate, and there are significant drivers in the ongoing climate change. Because of the many interactions of aerosols with there environment, enormous uncertainties exist. Moreover, aerosols have an effect on our health. Particles in the nanometer size range can get into our circulatory system, and this could lead to health issues. Due to the importance of these small particles regarding our climate and health, this thesis focused on the time evaluation of the particle size distributions (PSD) covering a size range of 3 nm to 900 nm, of the Viennese urban aerosol. To reach this aim it was necessary to combine two PSD, measured by a home-built two parallel differential mobility particle sizer (DMPS) measurement systems, to one particle size distribution. One of the DMPS system was operated with a Nano-differential mobility analyser (DMA). This system measured in a size range of about 3 nm to 40 nm. The other system was operated with a LongDMA and measured in a size range of about 10 nm to 900 nm. To combine these two PSDs, a calibration was executed with particles with a mobility diameter of 10 nm, 20 nm, and 30 nm. It turned out that PSDs measured with the parallel DMPS fit together for particles with a mobility diameter of 30 nm. The two parallel DMPs were used to measure the Vienna urban aerosol on the Faculty of Physics rooftop. The measurements were conducted over two weeks in January 2020. During this period, a commercial scanning mobility particle sizer (SMPS) measured at the same location in a size range from about 10 nm to 500 nm. The comparison showed that the time evaluation of the PSD measured with the two parallel DMPSS has a similar structure as the time evaluation of the PSD measured with the SMPS. During the measurement period, a new particle formation event could not be detected, Additionally, the total particle number concentration was measured during that period. A daily cycle can be observed from these measurements. Peaks could be identified during the morning- and the evening-rush hours as well as during lunchtime. The total concentrations measured with the SMPS had the same structure, but the particle number concentrations were lower compared to the measurements with the two parallel DMPS.

Zusammenfassung

Aerosole umgeben uns und können unser persönliches Leben auf unterschiedliche Weise beeinflussen. Es ist bekannt, dass Aerosole einen enormen Einfluss auf unser Klima haben und dass sie Treiber für den anhaltenden Klimawandel sind. Aufgrund der vielen Wechselwirkungen von Aerosolen mit ihrer Umgebung bestehen enorme Unsicherheiten. Darüber hinaus wirken sich Aerosole auf unsere Gesundheit aus. Partikel im Nanometerbereich können in unseren Blutkreislaufsystem gelangen und dies kann zu gesundheitlichen Problemen führen. Aufgrund der Bedeutung dieser kleinen Partikel für unser Klima und unsere Gesundheit konzentrierte sich diese Arbeit auf die zeitliche Entwicklung der Partikelgrößenverteilungen (PSD) des Wiener Stadtaerosols in einem Größenbereich von 3 nm bis 900 nm. Um dieses Ziel zu erreichen, war es notwendig, zwei PSD, gemessen mit einem selbstgebauten DMPS-Messsystem (Parallel Differential Mobility Particle Sizer), zu einer Partikelgrößenverteilung zu kombinieren. Eines der DMPS-Systeme wurde mit einem Nano-Differential Mobility Analyzer (DMA) betrieben. Dieses System hat in einem Größenbereich von etwa 3 nm bis 40 nm gemessen. Das andere System wurde mit einem Langen-DMA betrieben und hat in einem Größenbereich von etwa 10 nm bis 900 nm gemessen. Um diese beiden Größenverteilungen zu kombinieren, wurde eine Kalibrierung mit Partikeln mit einem Mobilitätsdurchmesser von 10 nm, 20 nm und 30 nm durchgeführt. Wie sich herausgestellt hat, sind die Halbwertsbreiten der Größenverteilungen für einen Mobilitätsdurchmesser von 30 nm am ähnlichsten zueinander, ausdiesem Grund wurden die Verteilung bei dem Mobilitätsdurchmesser von 30 nm zusammengefügt. Die beiden parallelen DMPS wurden verwendet, um das städtische Aerosol in Wien auf dem Dach der Fakultät für Physik zu messen. Die Messungen wurden über zwei Wochen im Januar 2020 durchgeführt. Während dieses Zeitraums wurde ein kommerzieller Scanning Mobility Particle Sizer (SMPS) an derselben Stelle in einem Größenbereich von etwa 10 nm bis 500 nm betriebn. Der Vergleich zeigte, dass die mit den beiden parallelen DMPSS gemessene zeitlichen Entwicklung der PSD eine ähnliche Struktur aufweist wie die mit dem SMPS gemessene zeitlichen Entwicklung der PSD. Während des Messzeitraums konnte kein Partikelneubildungsereignis festgestellt werden,Zusätzlich wurde die totale Partikelkonzentration in diesem Zeitraum gemessen. Es konnte ein täglicher Rhythmus festgestellt werden. Während des morgendlichen Verkehrs, zu der Mittagszeit und während des Abendlichen Verkehrs konnten erhöhte Konzentrationen festgestellt werden. Im Vergleich weist die totale Partikelkonzentration, die mit dem SMPS gemessen wurde, dieselbe Struktur auf, jedoch eine geringere Konzentration verglichen mit den Messungen des parallelen DMPS Systems.

Acknowledgements

First of all, I want to thank Prof. Paul Winkler for giving me the opportunity to work in his group. Paul Winkler supported me during my thesis and was always there if I needed a bit of good advice. In his group, I had the possibility to become acquainted with different research fields. I am so grateful to learn from such great and wisely colleagues.
I would particularly like to thank my colleagues Peter Wlasits, Paulus Bauer, Sophia Brilke, and Loic Gonzalez Carracedo. They showed me how prodigious it is to work in a scientific field. It was a pleasure to work and discuss with such great people.
Moreover, thanks to Harald Schuh and Julia Burkart not only for the fantastic assistance but also for furnishing the SMPS-Data and for servicing the SMPS during my measurements. I would also like to thank Prof. Bernadett Weinzierl and Nikolaus Fölker for lending me their nebulizer.
I would also like to thank my family for supporting me in many ways. My mother Sonja who is always there for me, who supported all my decisions during my studies, and who continues to believe in me. My sister Selina helped me a lot by supporting me in all private matters. Special thanks to my lovely husband, Mathias. He managed our life and gave me encouragement in every situation. He did everything so that I had time to concentrate on my academic work. Furthermore, I want to thank Tom Kästenbauer, my father in law, for giving me advice from an academic point of view and for having great discussions.
Moreover, I want to thank three great friends, namely Cristina, Alina, and Vici, whom I can totally rely on. I would also like to thank everyone who supported me during my master's thesis, especially my family and friends.

Contents

Chapter 1

Introduction

Following [1], aerosols are a collection of solid or liquid particles suspended in a carrier gas. A lot of different sub-categories of aerosols exist. One of the sub-categories are bioaerosols which arise from natural sources, that kind of aerosol includes viruses, fungi, and bacteria. Another relevant sub-category is smog. Smog is an essential part of the urban environment and generally less than 1 or 2 μm in size. Typically, an urban aerosol is found in the lowest kilometres of the atmosphere over cities. [1]

Urban aerosol is dominated by anthropogenic sources, for example smog [1] or industrial emissions [2]. The aerosol particle size distribution (PSD) is highly variable in the urban environment [2]. So, there can be extremely high concentration of particles, with less than 0.1 μm near a source, like a highway, but with distance, the concentration will rapidly decrease [2].

Today's society is confronted with one of the biggest problems in the 21^{st} century, the great acceleration. The great acceleration is characterized by observable nonlinear expansions, such as population growth, loss of species, heating the surface, pollution by greenhouse gases, and many more [3]. Generally, aerosols are part of the earth's environment, influencing our climate and interacting with our bodies. It is known that air pollution has a high impact on our health [4]. Especially in urban environments, humans and animals are exposed to air pollution due to anthropogenic emissions like industrial pollution and car emissions [4]. In the last decades, a lot happened in terms of adjustments [5]. Currently, the adjustments limit the pollution for micron size particles, but particles in a nanometer size range are not or insufficient regulated [6].To control ultrafine particles (<100 nm) is very important due to the fact that such particles may penetrate deeply into the lung [7]. Moreover, these ultrafine particles are able to reach our circulatory system [8]. By our circulatory system, the ultrafine particles can reach our organs like the liver, the heart, and the brain [8]. The legal guidelines set the focus on the mass of the aerosols, in such measurements are ultrafine particles generally underrepresented [6]. Therefore a particle size distribution would give more information about the current situation in our air, regarding the particle number concentration and the size of the aerosols [6].

Moreover, aerosol can influence our climate in different ways. According to [9], an example of how aerosols are affecting our climate is the radiative forcing (RF) (W m^{-2}). RF is the change in energy flux caused by drivers, for example aerosols, and is calculated at the top of the atmosphere. The effective radiative forcing (ERF) is the result of calculations of RF for well-mixed greenhouse gases and aerosols, respond to perturbation with rapid adjustments. ERF has two

types of interaction. One is the effective radiative forcing from an aerosol-radiation interaction (ERFari), and the other is in the form of the effective radiative forcing from an aerosol-cloud interaction (ERFaci). These interactions can be seen schematically in Figure 1.1. The ERFari describes the effects of interactions direct on aerosols, for example, the scattering or absorption on an aerosol. The ERFaci describes the effects of interactions with clouds. [9]

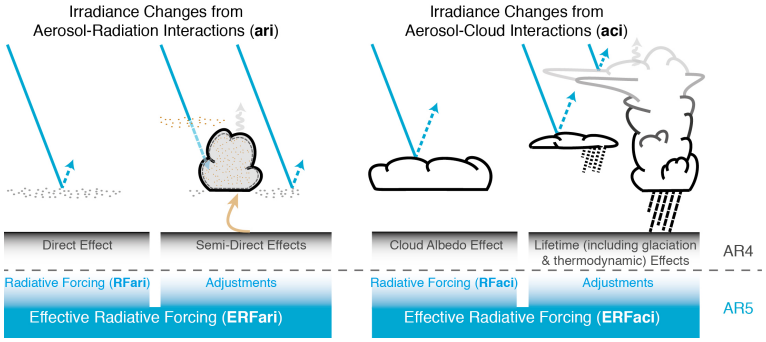

Figure 1.1: Schematic explanation of the effective radiative forcing [9].

According to [9], due to the different effects, aerosols generally have a cooling or a heating effect. The cooling effect generally comes from the scattering of light on aerosols and clouds. Contrary to the cooling effect, the heating effect is generated by the absorption of light. In Figure 1.2 the RF depended on different atmospheric constituents are shown. Because of many interactions between aerosols with, e.g., clouds and greenhouse gases, enormous uncertainties in terms of climate impact exist. [9]

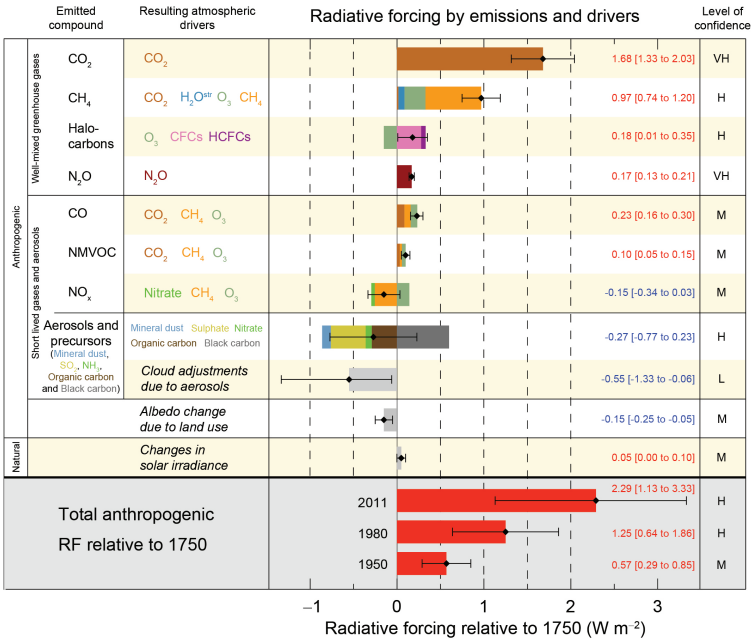

Figure 1.2: Anthropogenic radiative forcing estimates and aggregated uncertainties for the main drivers of climate change [10].

In view of the importance of ultrafine particles regarding our climate and our health, this thesis focused on the time evaluation of the PSD covering the size range of 3 nm to 900 nm

in the urban environment of Vienna. To cover this size range it is necessary to combine two PSD measured with two differential mobility particle sizer (DMPS) systems, which operate with differential mobility analyser (DMA)s to get complete PSD of the Vienna Urban air, covering the size ranges 3 - 40 nm and 10 - 900 nm, respectively. For combining the two PSDs, it is necessary to calibrate the system in the overlapping size ranges. To this end, aerosols with a well-defined mobility size were produced. The measurements for the time evaluation of the PSD of Vienna urban aerosol took place at the University of Vienna's Faculty of Physic's rooftop laboratory. This laboratory is situated within the physics building's attic and approximately 35 m above ground [11]. The laboratory is separated from major traffic routes therefor background measurements, and long-term measurements of the Viennese urban aerosol are possible [11].

Chapter 2

Theoretical Background

According to [1,12], it is essential to understand the interaction between particles and their carrier gas. The classical kinetic theory of gases describes this well. The basic hypothesis of the kinetic gas theory is,

1. gases contain a large number of molecules,
2. molecules are small compared to the distances between them,
3. and, the molecules are rigid spheres travelling in straight lines between each elastic collision.

In this theory, many parameters can be described. A few examples are pressure, temperature, the mean free path, diffusion, and many more. The ideal gas law is relevant for most gases, including air. This law describes how the absolute pressure P, the absolute temperature T, the volume V, and the number of moles n of a gas are related

$$PV = n \cdot R \cdot T. \tag{2.1}$$

This law is a combination of Boyle's law, Charles's law, and the Avogadro's principle. Boyle's law describes that the pressure multiplied with the volume of an ideal gas is constant,

$$P \cdot V = const. \tag{2.2}$$

which means that n and T have to be constant as well. [1, 12]
Following [2], the thermodynamic behaviour of aerosols is given by the Gibbs free energy. The Gibbs free energy is a useful parameter because of the temperature and the constant pressure, it refers to the nucleation processes. The Gibbs free energy G is given by

$$G = U + pV - TS. \tag{2.3}$$

In this equation, U refers to the internal energy, p to the pressure, T is the temperature, and S refers to the system's entropy. Equation 2.4 describes a state by using the total derivation of the Gibbs free energy

$$dG = -SdT + Vdp + \mu_i dn_i. \tag{2.4}$$

Here μ_i refers to the chemical potential. For a system with constant temperature, pressure, and chemical composition, $dG = 0$ which describes the stable equilibrium of a state. [2]

2.1 Nucleation

2.1.1 Homogeneous nucleation

As reported in [1], homogeneous nucleation is the formation of new particles from a supersaturated vapor, excluding the interaction with condensation nuclei or ions. It is also called self-nucleation. [1]
Following [2], the saturation ratio, for the degree of supersaturation of a solute, at temperature T is defined as:

$$S = \frac{p_A}{p_A^s(T)} \tag{2.5}$$

where p_A is the partial vapor pressure of solute A and $p_A^s(T)$ is the saturation vapor pressure of A in equilibrium with its liquid phase at temperature T. There are three existing cases of a saturation ratio,

1. if $S < 1$ then the vapor is unsaturated,
2. if $S = 1$ then the vapor is saturated,
3. if $S > 1$ than the vapor is supersaturated.

A saturated vapor or an unsaturated vapor may become a supersaturated vapor by undergoing thermodynamic processes, for example isothermal compression or adiabatic expansion. [2]

Kelvin effekt

In line with [2], Equation 2.6 is an expression for the Gibbs free energy

$$\Delta G = -\frac{4}{3}\pi R_p^3 \frac{kT}{\nu_l} ln(S) + 4\pi R_p^2 \sigma. \tag{2.6}$$

Here k refers to the Boltzmann constant, R_p is the droplet radius, σ refers to the surface tension of the droplet and ν_l is the volume occupied by a molecule in the liquid phase. If the vapor is unsaturated both terms of Equation 2.6 on the right hand side (RHS) are positiv. In this case ΔG increases with R_p.
If the vapor is supersaturated, the first term on the RHS of Equation 2.6 will be negative. Therefore, for particles with small R_p, the surface tension term dominates and the ΔG behavior is similar to the case of $S < 1$. If R_p increases, the first term on the RHS becomes more important. For that case ΔG reaches a maximum value of ΔG^* at $R_p = R_p^*$. The radius can be calculated by setting $\frac{\partial \Delta G}{\partial R_p} = 0$, which leads to

$$R_p^* = \frac{2\sigma\nu_l}{kTln(S)}. \tag{2.7}$$

R_p^* is called Kelvin radius. Equation 2.7 and the saturation ratio can be used to express the $Kelvin\ equation$

$$p_A = p_A^S(T) exp\left(\frac{2\sigma\nu_l}{kTR_p}\right). \tag{2.8}$$

The Kelvin equation is valid for homogeneous and heterogeneous nucleation. The Kelvin equation characterizes equilibrium conditions over curved surfaces, moreover the equilibrium can only be maintained if S > 1. Additionally, it shows that the saturation ratio over a curved droplet surface is always higher than over a flat surface.
The free energy barrier height which is based on the $Kelvin\ equation$ is defined as,

$$\Delta G_{hom}^* = \frac{4\pi}{3}\sigma R_p^{*2} = \frac{16\pi}{3}\frac{\sigma^3\nu_l^2}{(kTlnS)^2}. \tag{2.9}$$

From Equation 2.9 it is known that if the saturation ratio increase, the ΔG_{hom}^* and the critical radius will decrease. [2]

2.1.2 Heterogeneous nucleation

In contrast to homogeneous nucleation, heterogeneous nucleation is a particle formation growth process which is promoted by the presence of condensation nuclei or ions [1].
Following [2], heterogeneous nucleation takes place at lower supersaturations than homogeneous nucleation. The heterogeneous nucleation rate is defined as the number of critical nuclei appearing on a unit surface per unit time, for a liquid droplet on an insoluble foreign surface. For the case of a flat surface, the free energy of a critical cluster formation is defined as

$$\Delta G^* = \Delta G_{hom}^* f(m) \tag{2.10}$$

where ΔG_{hom}^* is the free energy of homogenous critical nucleus formation, and m is the contact parameter. [2]
According to [13], the Young equation relates the contact parameter to the surface tension

$$m = cos(\Theta) = \frac{\sigma_{SV} - \sigma_{SL}}{\sigma_{LV}}. \tag{2.11}$$

Here S represents the substrate, V the gas phase, and L the liquid phase of the nucleus. As shown in Figure 2.1, Θ is the contact angle between the nucleus and the substrate. [13]

The function $f(m)$ is given by

$$f(m) = \frac{1}{4}(2+m)(1-m)^2 \tag{2.12}$$

If the contact angle $\Theta = 0$, $f(m) = 0°$ and nucleation begins as soon as the vapour is supersaturated, the surface's wettability is maximal. When the contact angle $\Theta = 180°$ and $f(m) = 1$, heterogenous nucleation is not favored over homogenous nucleation. [2]

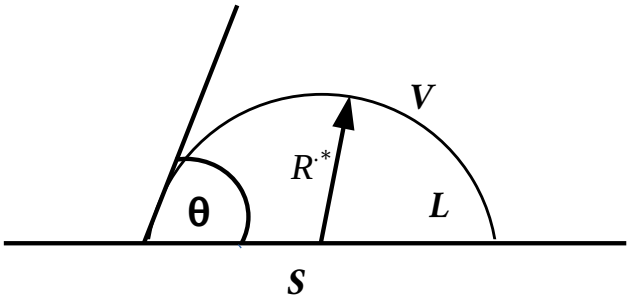

Figure 2.1: Schematic heterogeneous nucleation on a flat surface [2].

As reported by [14], in the case of heterogeneous nucleation on a curved surface, free energy is a necessary condition to achieve formation of an embryo with a critical radius R^* on a spherical nucleus with a radius R, which is given by

$$\Delta G^* = \Delta G^*_{hom} f(m,x) \qquad with \quad x = \frac{R}{R^*}. \tag{2.13}$$

Contrary to heterogeneous nucleation on a flat surface, the contact angle and the radius of the seed particle is relevant, which is shown in Figure 2.2. Insoluble particles are good sites for nucleation for small contact angles, while larger contact angles inhibit nucleation. [14]

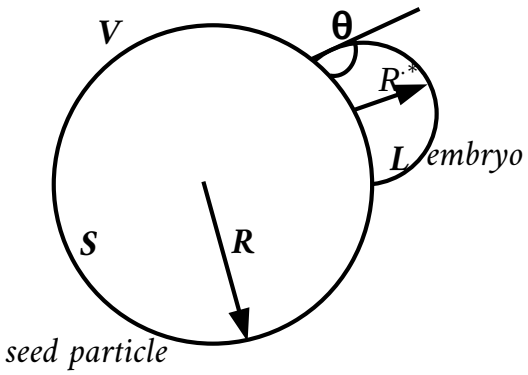

Figure 2.2: Schematic heterogeneous nucleation on a curved surface [13].

2.1.3 Condensation

According to [1], growing by condensation starts when a stable droplet is formed. The growth rate depends on the saturation ratio, particle size, and particle size relative to the carrier's gas mean free path. If the particle size is less than the mean free path, the growth will depend on the random molecular collisions between them and the vapor molecules. In a stationary gas the

number of molecular collisons per unit area per second is defined as

$$z = \frac{n\overline{c}}{4} \tag{2.14}$$

where $\overline{c}$ is the mean molecular velocity and n is the concentration of molecules.

$$\overline{c} = \left(\frac{8RT}{\pi M}\right)^{\frac{1}{2}}. \tag{2.15}$$

Where M is the molecular weight of the gas.

$$n = \frac{p_\infty}{kT}. \tag{2.16}$$

Here p_∞ is the pressure of the ideal gas law. Using the description for $\overline{c}$ and n, z is defined as:

$$z = \frac{p_\infty}{\sqrt{2\pi mkT}} \tag{2.17}$$

where m is the mass of the vapor molecule. This equation describes the rate of arrival of vapor molecules per unit area of the droplets surface. To illustrate particle growth, it is necessary to account for molecules that leave the surface by evaporation and those that do not stick

$$\frac{d(d_p)}{dt} = \frac{2M\alpha_c(p_\infty - p_d)}{\rho_p N_a\sqrt{2\pi mkT}}, \qquad for \quad d_d < \lambda \tag{2.18}$$

where m is the mass of the vapor molecule, p_d refers to the partial pressure at the droplet surface, ρ_p describes the density of the liquid, N_a is the Avogadro's number,α_c refers to the condensation coefficient and λ to the mean free path. [1]
Following [1], if the particle size is larger than the mean free path, the growth will not depend on the rate of random collisions, but on the rate of diffusion of molecules to the droplet surface. The following equation defines the rate of particle growth for a single droplet of pure liquid

$$\frac{d(d_p)}{dt} = \frac{4D_v M}{\rho_p d_p R}\left(\frac{p_\infty}{T_\infty} - \frac{p_d}{T_d}\right)\psi, \qquad for \quad d_d > \lambda \tag{2.19}$$

where D_v is the diffusion coefficient of the vapor, T_∞ is the temperature away from the droplet surface, T_d the surface temperature and ψ is the Fuchs correction factor. [1]

2.2 Size distribution

Following [1], the size of a monodisperse particle can be fully defined by the particle diameter. Most environmental aerosols, as well as the urban aerosol, are polydisperse, and the particle size can be spread over a range of two or more orders of magnitude. Therefore, and since the physical properties of aerosols strongly depend on the particle size, it is essential to describe the size distribution by statistical means. Most distributions are characterized by either their centre or their width.

A common particle size distribution in aerosol physics is the lognormal distribution. This function is symmetrical and fits perfect to a monodisperse aerosol. The number frequency function is defined as:

$$df = \frac{1}{\sigma\sqrt{2\pi}} exp\left(-\frac{(d_p - \overline{d_p})^2}{2\sigma^2}\right) dd_p. \tag{2.20}$$

Where d_p is the diameter of the particle, $\overline{d_p}$ is the arithmetic mean diameter of the particles, σ is the standard deviation. The commonly used statistical parameters are the arithmetic mean of $ln(d_p)$, called the geometric mean diameter, and the standard deviation of the logarithm σ_g, called geometric standard deviation. The geometric mean diameter is defined as,

$$ln(d_g) = \frac{\sum n_i ln(d_i)}{N}. \tag{2.21}$$

Here N is the total number of particles, n_i are the particles in the group i and d_i is the arithmetic midpoint. The geometric standard deviation is defined as

$$ln(\sigma_g) = \left(\frac{\sum n_i (lnd_i - lnd_g)}{N-1}\right)^{1/2}. \tag{2.22}$$

[1]

2.3 Urban Aerosol

According to [2], urban aerosol is a mixture of primary emissions from, for example, industries, transportation, and secondary material formed by the mechanisms that are described above. The number particle distributions are dominated by particles smaller than 100 nm. [2]
In agreement with [1], Figure 2.3 presents three modes of an urban aerosol. The nuclei mode consists of aerosols from primary sources and particles formed in the atmosphere through gas to particle conversion. That mode is usually found near highways. Because of the aerosol size, these particles coagulate rapidly with each other and with particles of the accumulation mode. For that reason and high number concentration, particles in that mode have a relatively short atmospheric lifetime. The nuclei mode turns into in the accumulation mode. The accumulation mode consists of particles in a size range of the visible light, like smog. The coarse particle mode includes, for example, mechanically generated anthropogenic particles. Because of sedimentation, they have a relatively short lifetime in the atmosphere. [1]

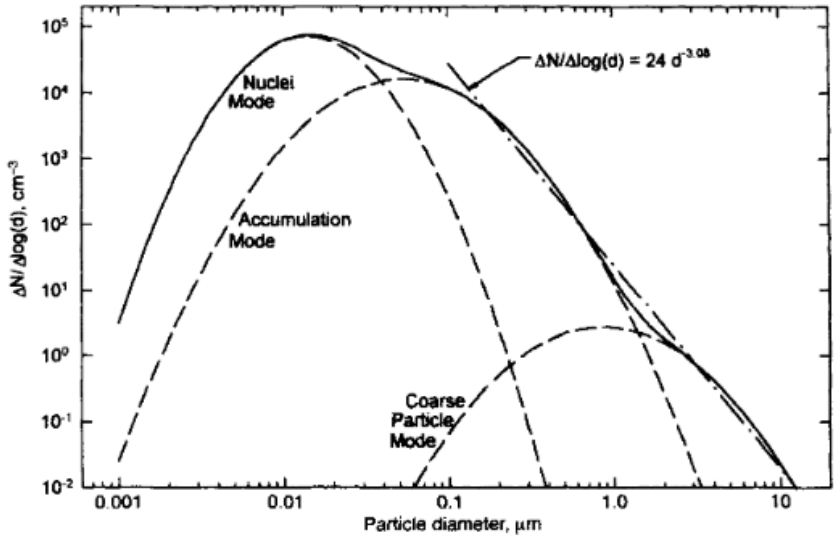

Figure 2.3: Particle number distribution from an urban surrounding [1] page 309.

2.4 New particle formation

The formation of thermodynamically stable clusters, from homogeneous nucleation followed by growth by condensation and coagulation of these clusters, is called new particle formation (NPF) [15].

According to [16], this effect is a two-step process. The first step includes the homogeneous nucleation of thermodynamically stable clusters. The second step includes the growth of these clusters by condensation and coagulation into quasi-stable aerosols. Under tropospheric conditions, sulfuric acid, water, and ammonia are the most relevant nucleating species for forming clusters of about 1 nm. [16]

The occurrence of NPF events can affect the aerosol particle number concentration [17]. NPF and the term $growth\ event$ describes the formation of a new particle mode and the particle growth to larger sizes, detectable with continuous size distribution measurement methods at the smallest sizes around 1-2 nm [15]. NPF events are highly influenced by meteorological conditions, for example, wind and photochemical reactions of precursor gases [18]. Commonly accepted, a NPF event has the shape of a $banana$ [19].

In general NPF events are characterized by their frequency, intensity, and the growth rate of the newly formed particles [15]. The frequency of such events depends, in most cases, on the season [15]. There are often fewer events during winter periods [15]. NPF events can be observed in many different regions, for example in high mountain regions [20], in the boreal forest [21], and also in urban areas [22, 23].

Many studies pointed out that organic substances are massive drivers for secondary particle formation [21]. In particular, these substances are essential for the growth of clusters in the nanometer size range [16]. Furthermore, many studies demonstrated an increased rate of formation with higher concentrations of organic substances under laboratory conditions [24].

The composition of ambient air plays an essential role in the formation of new particles [25]. In urban areas, the direct emission, by traffic and industry, of ultrafine particles contributes to the particle composition and number concentration [25]. In the urban environment, NPF is a

significant contributor to urban smog [26]. Due to the different components of urban air and their minute quantities, revealing of the mechanisms how NPF events take place is extremely challenging. [27]. [28] pointed out, that nitric acid and ammonia has the potential to drive rapid particle growth.

Classification

The classification of NPF events is based on the scheme described by [29]. A NPF event is identified if a new mode of aerosol particles can be observed in the nucleation mode size range. This size range is commonly smaller than 25 nm. Additionally, the structure must show a growth pattern for several hours. An example of an $event$ can be seen in Figure 2.4. Here a new mode occurs during lunchtime. This event starts at a particle diameter of about 15 nm and growth to a particle diameter of about 40 nm over several hours. If a growing mode can not be observed, that day is defined as a $non\ event$. For days that did not fulfil all event criteria, but some, that day is classified as $undefined$. [29]

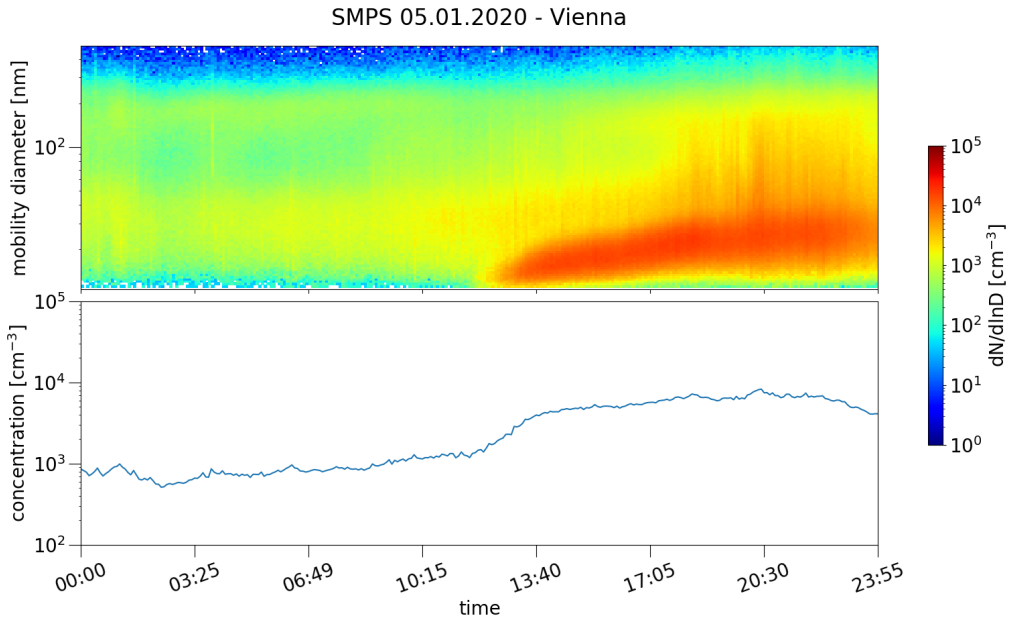

Figure 2.4: The upper plot shows the time evaluation of the PSD of the Vienna urban aerosol. The colours represent the particle number concentration, the axis of abscissas represent the hours of January 05, 2020 and the axis of the ordinate the mobility diameters. In the lower plot, the total particle number concentration is shown. The time evaluation of the PSD and the total particle number concentration were recorded with a commercial SMPS, located at the rooftop of the faculty of physics.

The Viennese aerosol is the subject of many studies [11, 22, 30]. In 2007/2008, the average total particle concentration was 7300 cm^{-3} [30]. For comparison, the median of the daily particle concentration in 2008/2009 was 10600 cm^{-3} in Budapest, and 7300 cm^{-3} in Prague [31]. According to [22], during longterm measurements between 2012/2013, 51 days of 443 classified as an $event$, in Vienna. Measurements were taken on 116 days in winter, only three days were classified as an $event$. [22]

Chapter 3

Experimental Setup

3.1 Instrumentation

3.1.1 Aerosol charging

For measurements based on electric mobility, the aerosols must have a well defined charging state for the electrical mobility spectrometer (EMS) [32]. For getting a well defined stable charging state, different charging methods can be used [33]. In this master thesis, two different bipolar chargers were used, first a americium-241 (^{241}Am) and second a soft X-ray charger.
Following [33], the ^{241}Am charger has a cylindrical geometry with an axial flow direction, shown in Figure 3.1. The aerosol inlet and the aerosol outlet are cone-shaped. [33]
According to [32], within the cylinder, the ^{241}Am source is implanted on a gold matrix coated strip and housed in a stainless steel body. This radioactive source has an activity of 60 MBq. [32]
The TSI Model 3088 [34], an advanced aerosol neutralizer, was the second charger in use. This

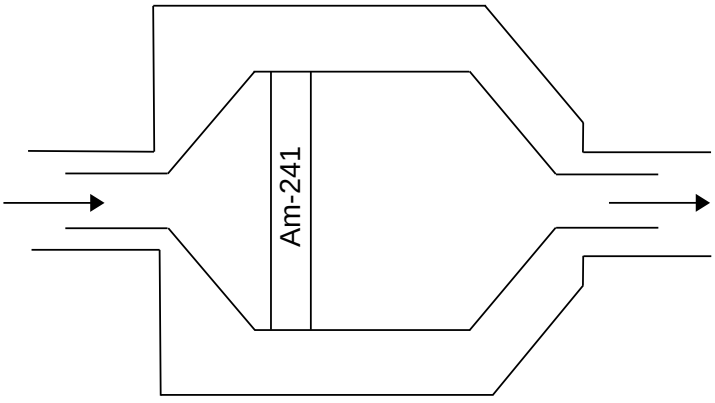

Figure 3.1: Schematic sketch of an ^{241}Am charger [33].

charger is a soft X-ray charger [34]. Generally spoken, a soft X-ray charger produces radiation with wavelengths in the order of 0.1 nm and with photon energy up to 10 keV [33].
As reported by [33], the aerosol enters the stainless steel tube on its axis and flows through the tube, shown in Figure 3.2. The source is placed at the end of the tube. After passing the source, the aerosol leaves the charger through an outlet oriented perpendicularly to the tube's axis. [33]

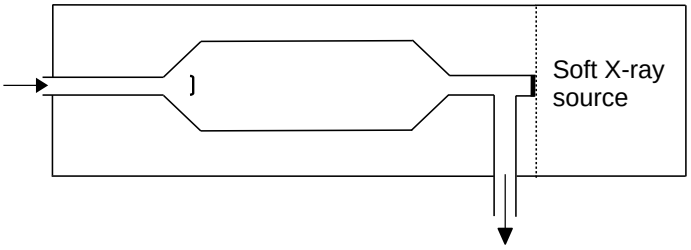

Figure 3.2: Schematic sketch of the used soft X-ray charger [33].

3.1.2 Differential mobility analyser

A DMA can be used to generate monodisperse aerosol and to determine a particle size distribution [35]. In this master thesis, a Vienna-TypeDMA ([36], [37]) was used. To quantify a DMA the geometry parameters and the flow parameters were used. Especially two NanoDMAs and one LongDMA were used in this thesis. In table 3.1 the geometry of the used DMAs are shown. Following [38], the characteristic geometry of the capacitor in this DMA type is a cylinder, shown

	NanoDMA	LongDMA
R_1	17.5 mm	18.0 mm
R_2	24.1 mm	25.0 mm
L	15 mm	600 mm

Table 3.1: Geometry of the DMAs.

in Figure 3.3. The aerosol has to be charged before it is entering the DMA. A laminar flow of clean sheath air transports the sample flow axially between the central rod and the coaxial tube. The coaxial tube is grounded, and the voltage on the central electrode is set between 20 V and 10000 V. There is a gap near the rod's bottom, which allows selected aerosols to leave the DMA. Only particles with a narrow range of mobilities can enter this gap. Particles with greater mobility will migrate to the rod's central walls, particles with lower mobility flow beyond the gap and leave the DMA with the sheath air. The exit aerosol sample flow is nearly single charged and roughly monodisperse. The size of the particles is controlled by adjusting the voltage on the central rod.

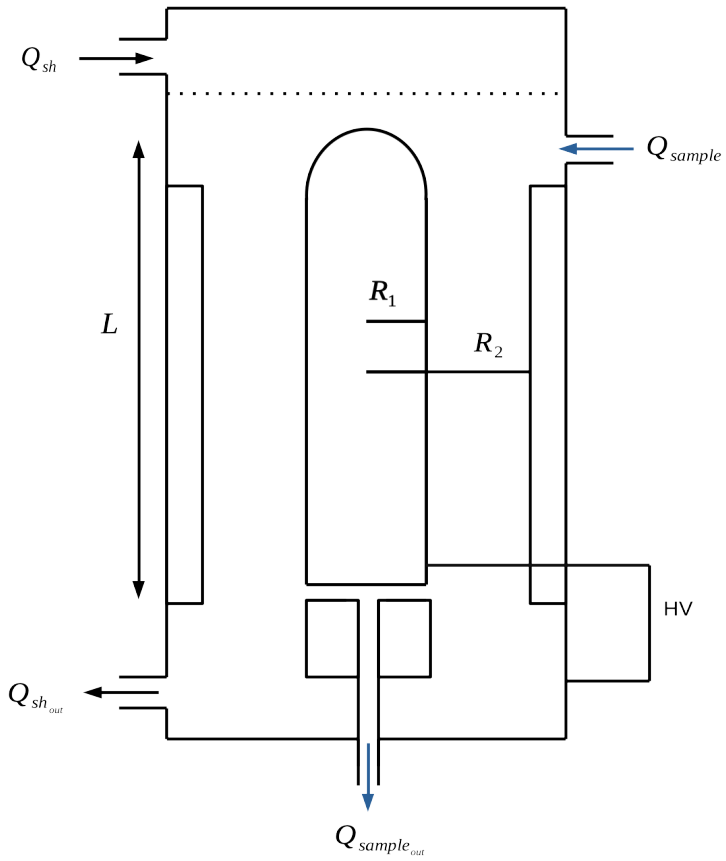

Figure 3.3: Schematic Vienna type DMA: following [38] the geometry parameters are R_1 the radius of the central rod, R_2 the radius of the coaxial tube, and L is described as the distance between the aerosol inlet and the outlet. Marked with a blue arrow are the aerosol flow rate Q_{sample} and the sample flow rate $Q_{sample_{ex}}$. Marked with black arrows are the sheath air flow rate Q_{sh} and the sheath excess airflow rate $Q_{sh_{ex}}$. [38]

The following equation gives the relation between the applied voltage and the electrical mobility

$$Z = \frac{1}{V} \frac{ln\left(\frac{R_2}{R_1}\right)}{2\pi L} \frac{(Q_{sh} + Q_{sh_{ex}})}{2} \tag{3.1}$$

In addition the electric mobility of a spherical particle can be expressed as

$$Z = \frac{ie_0}{3\pi\eta} \frac{C(d_p)}{d_p} \tag{3.2}$$

where e_0 is the elementary charge, η is the dynamic viscosity of the carrier gas, d_p is the mobility equivalent diameter and $C(d_p)$ is the Cunningham slip correction factor. [38]

The Cunningham slip correction factor is defined as:

$$C(d_p) = 1 + \frac{\lambda}{d_p}\left(2.492 + 0.840 * e^{-0.430\left(\frac{d_p}{\lambda}\right)}\right). \tag{3.3}$$

[38]
For the carrier gas air, the mean free path is λ_{air} = 67.3 nm and dynamic viscosity η_{air}= 1.83*10^{-5} Pas at 23°C and 1013 Pa [39]. To calculate the voltage which has to be applied for a specific mobility diameter, the equations Equation 3.1 and Equation 3.2 have to be set equal.

3.1.3 Condensation particle counters

According to [1], there are many options for particle detection. Condensation particle counters are the standard option for detecting the number concentration. All common condensation particle counters (CPC)s use water or alcohol as working fluid. The evaporation of these fluids is used to saturate the incoming aerosol, here a wick assisted. After saturation, the aerosol-flow must be cooled down by an adiabatic expansion or non-isothermal diffusion. The cooling process is necessary to generate a level of supersaturation, which is required for particle growth. After the growth process, the number concentration is usually measured by optical detection, seen in Figure 3.4. [1]
In this thesis, only the TSI 3776 CPC [40] was used. This CPC uses n- butanol as working fluid [41].

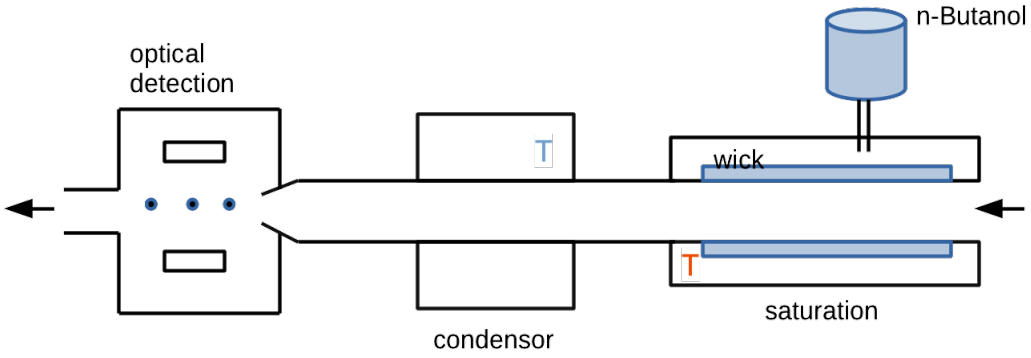

Figure 3.4: Schematic CPC: right is the aerosol inlet marked with a black arrow. The saturation section operates with warmer temperatures (red T) as the condenser (blue T) [41]

3.2 Calibration of the combined PSD

The calibration set-up is shown in Figure 3.5. The aerosol, a Natriumchlorid (NaCl) solution, was generated with a nebulizer similar to [42]. The NaCl solution had an amount of substance of

$$n = \frac{m}{M} = \frac{0.1g}{58.44g/mol} = 0.001711mol \tag{3.4}$$

The sprayed NaCl solution passed a dryer, and a ^{241}Am charger with a flow rate of 6.1 l per min. After the charger, the aerosol was selected with the NanoDMA-1. The NanoDMA-1 had a

sheath flow rate of 19.3 l per min. With NanoDMA-1 particles with a mobility diameter of 10 nm, 20 nm, and 30 nm were selected. After the selection, the monodisperse aerosol split up. On the one hand, the flow ended in the reference CPC. This CPC was used to detect the total concentration during the measurements. On the other hand, the flow split up to two parallel DMPS [43] systems.

Generally, in a DMPS system, the aerosol passes a charger, a DMA, and ends up in a detecting system. For charging the monodisperse aerosol, a ^{241}Am charger was used. One of these systems worked with the NanoDMA-2, with a sheath flow rate of 18.5 l per min. This system is called NanoDMPS. The other DMPS system worked with a LongDMA, with a sheath flow rate of 8 l per min. This system is called LongDMPS. In both cases, the aerosol ends up in a butanol CPC TSI 3776 [40].

To cover with the NanoDMA the size range of about 3 nm to 40 nm and with the LongDMA the size range from about 10 nm to 900 nm, consequential the sheath-flow rates for the NanoDMA and the Long DMA were chosen as shown in Table 3.2. The aerosol flow is determined by the flow specifications of the respective CPCs.

DMA	$Q_{sh} = Q_{sh_{ex}}$ [l/min]	$Q_{sample} = Q_{sample_{ex}}$ [l/min]
NanoDMA -1	19.3	6.1
NanoDMA -2	18.5	1.5
LongDMA	8.0	1.5

Table 3.2: Flow parameters of the used DMAs.

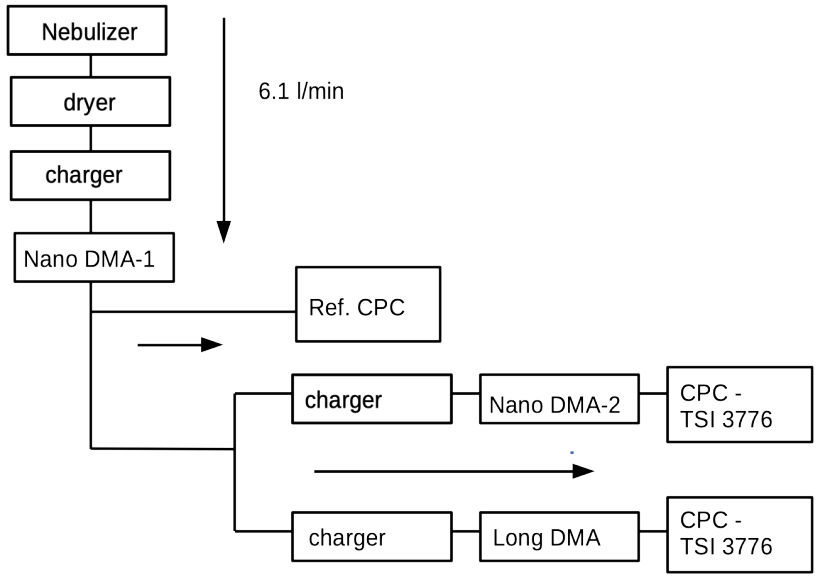

Figure 3.5: Setup for the calibration measurements.

The following steps were done for the calibration measurements:

- create a NaCl solution, fill it in the nebulizer, and turn on the synthetic air,

- turn the CPCs on and wait until they are warmed-up,
- switch the pumps for the DMA on,
- check all flow rates with a flowmeter [44] and readjust it,
- do zero measurements, to check the DMAs. The zero measurements were made by putting zero voltage on the central electrode of the DMA and by measuring the concentration behind the DMA with a CPC. If the DMA is clean and theQ_{sh} is equal to $Q_{sh_{ex}}$, the CPC detects zero particles,
- turn on the EMS-Program [45] [46]
- set the voltage on the central electrode of NanoDMA-1 to select the particles with a specific mobility diameter, here the EMS -10 Control Center Operating Software EMSCC 1.4 was used for the classifier

particle mobility diameter	voltage on the central electrode [V]
30 nm	509.54
20 nm	1980.51
10 nm	4329.95

Table 3.3: Voltage on the central electrode of NanoDMA-1 with the sheath-flow rate of 19.3 l/min at the specific particle mobility diameter

- the EMS -10 Control Center Operating Software EMSCC 1.4 was used as well as for the analyzer, to measure a PSD
- start the analyzer to control the voltage on the central electrode of the NanoDMA-2 and the LongDMA,
- record with the Software, for every selected particle diameter, the particle concentration with the CPCs behind the DMAs and the total concentration with the Ref-CPC,

3.3 Rooftop measurements of the Vienna Urban Aerosol

The rooftop laboratory is situated in the attic of the Faculty of Physics of the University of Vienna, around 35 m above ground [11]. The experimental setup for the rooftop-laboratory-measurements is schematically shown in Figure 3.6. The Vienna urban aerosol was selected with an inlet and had an aerosol-flow rate of 4.5 l/min, shown in Figure 3.7. After this inlet, a T-junction was used to create a two-way flow. In one way, the aerosol flow ends up in a reference CPC, which detected the total number concentration during the measurements. The other way split up by using a T-function to create a two-way flow. In each course was a DMPS system located. One of these DMPS systems was a NanoDMPS, the other was a LongDMPS. The PSD measured by the NanoDMPS was in a size range from 2.97 nm to 46.77 nm. The PSD measured

by the LongDMPS was in a size range from 11.73 nm to 931.80 nm.

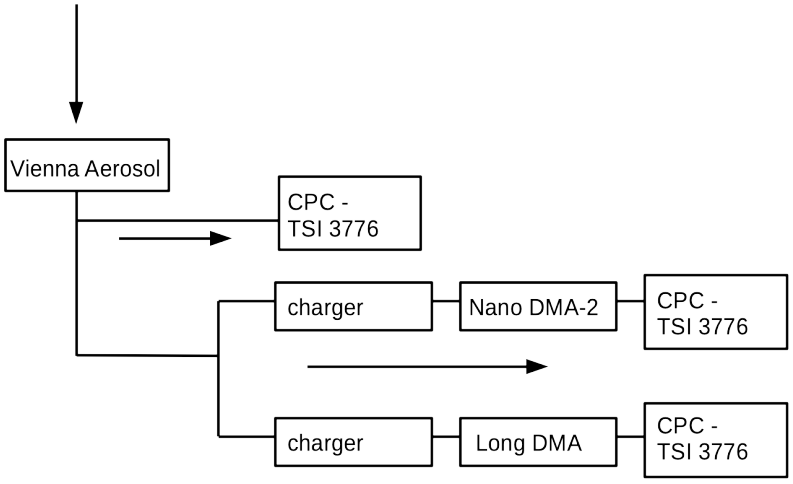

Figure 3.6: Schematic setup for the rooftop measurements.

Figure 3.7: Inlet for the Vienna urban aerosol

To set the voltage on the central electrode of each DMA and record the particle number concentration, detected by the CPCs, a EMS program for each DMPS was used. The time resolution of the NanoDMPS is about 10 minutes, and the time resolution of the LongDMPS is about 20 minutes.
From January 22, 2020, to February 6, 2020, the time evolution of the particle number size distribution was measured with the system described above. The total number concentration measured with the Ref-CPC was recorded with a program called Aerosol Instrument Manager (AIM) [47].

Chapter 4

Data evaluation

4.1 Calibration of the combined PSD

For the calibration, a few runs were recorded with the EMS-program. For the NanoDMPS (green) and the LongDMPS (blue), for every selected particle size, a PSD was measured, shown in Figure 4.1.

To determine the PSD of the NaCl aerosol for the specific selected mobility diameter, the

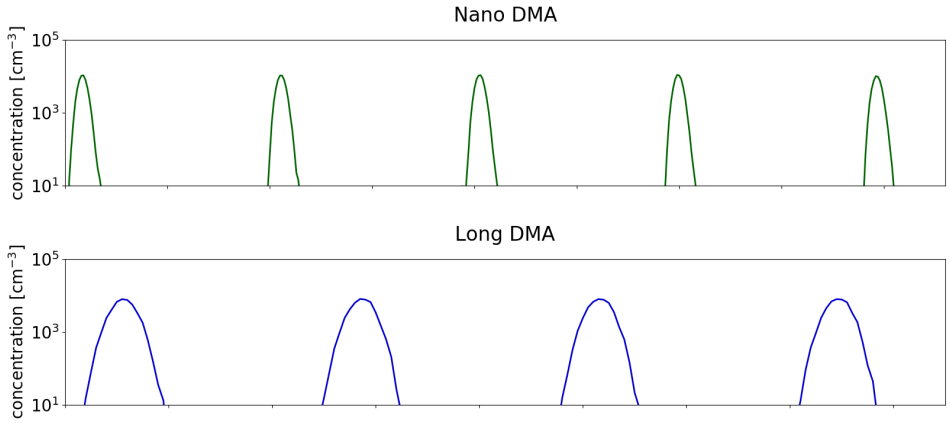

Figure 4.1: Exemplary raw data: the green data represents the runs of the NanoDMPS, the blue data represents the runs of the LongDMPS. The axis of abscissas represents the time of the specific run.

particle number concentration for every mobility diameter was averaged. After plotting the averaged particle number concentration against the particle mobility diameter, the full width at half maximum (FWHM) was calculated of every distribution, to compare the NanoDMA-2 and the LongDMA. The calibration plots are shown in Figure 4.2. The top graphics represent the measured curves for the selected 30 nm particles. Green represents the PSD measured with the NanoDMPS-2, and blue represents the PSD measured with the LongDMPS. The calibration plots for the selected 20 nm particles are shown in the middle. The mobility diameter of the 10 nm particles is represented in the last row.

The calibration data of the LongDMPS with a mobility diameter of 10 nm, can be neglected because the EMS-program was not able to set the exact voltage. On the axis of abscissas, the particle diameters are plotted, and on the axis of the ordinate, the particle number concentration.

The peaks from the curves are around the selected particle diameters, seen in Table 4.1.

As seen in Table 4.2 the FWHM of the PSDs and the mean diameters are more similar for

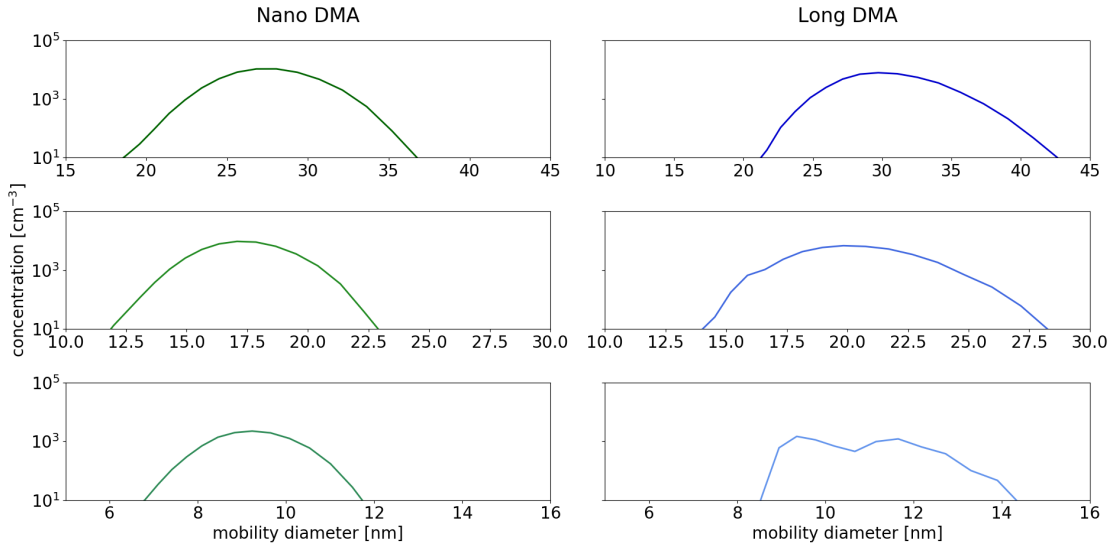

Figure 4.2: Calibration, in green: the PSD measured by the NanoDMPS and in blue: the PSD measured by the LongDMPS.

	NanoDMA	LongDMA
at 30 nm	26.71 nm	29.73 nm
at 20 nm	17.92 nm	19.84 nm
at 10 nm	9.24 nm	/

Table 4.1: Mobility diameter at the center of the distribution.

particles with 30 nm, than with 20 nm. Thus, the PSD of the two parallel DMPS systems will be combined at a mobility diameter of 30 nm.

	NanoDMA	LongDMA
at 30 nm	FWHM= 4.70 nm	FWHM= 5.16 nm
at 20 nm	FWHM= 4.72 nm	FWHM= 5.45 nm
at 10 nm	FWHM= 4.59 nm	/

Table 4.2: FWHM of the calibration size distributions.

4.2 Rooftop measurements of the Vienna Urban Aerosol

4.2.1 Total concentration

The total concentration was measured with the reference CPC, during the measurements located at the rooftop laboratory. Here a CPC 3776 from TSI [40] was used. The particle number concentration was recorded with the AIM-program [47]. This program records the particle number concentration each second. An exemplary cutout of this data can be seen in Figure 4.3.
The total concentration for the weekly cycle was calculated by averaging the hours of each day.

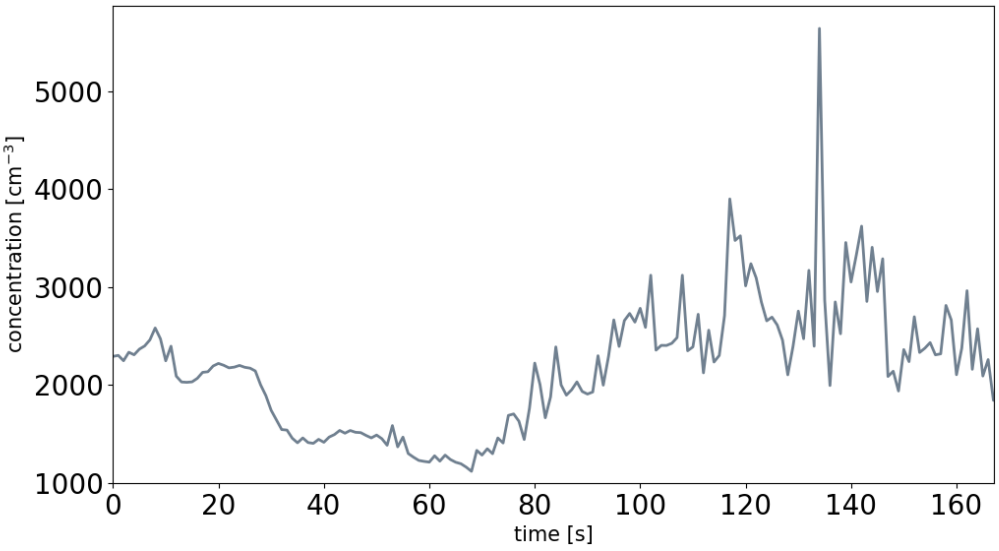

Figure 4.3: Exemplary raw data of the total concentration.

4.2.2 Time evaluation of the particle size distribution

The particle number concentration was calculated with a program from my colleague Carl Tondel. The program's code is based on [48].
The time evolution of the PSD measured by the LongDMPS is shown in Figure 4.4. This PSD is in a mobility size range of 11.73 nm to 931.80 nm. Here the color represents the particle number concentration. Red is an indicator for high concentrations, and blue represents low concentrations. The axis of abscissas represents the time of a specific day, and the axis of the ordinate, the mobility diameters.

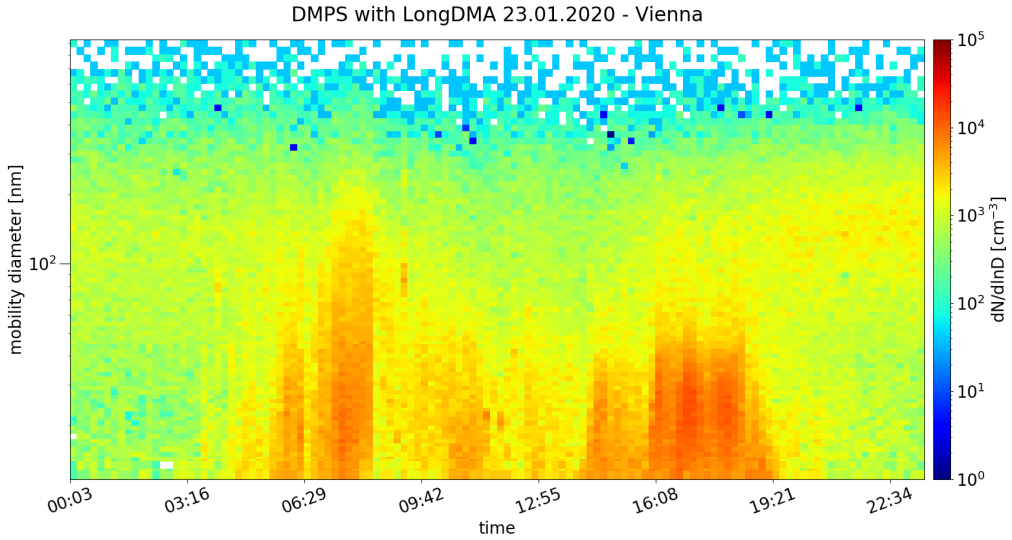

Figure 4.4: Exemplary time evaluation of the PSD measured by the LongDMPS.

In Figure 4.5 the time evaluation of the PSD is shown, measured by the NanoDMPS. This PSD is in a mobility diameter size range of 2.97 nm to 46.77 nm.

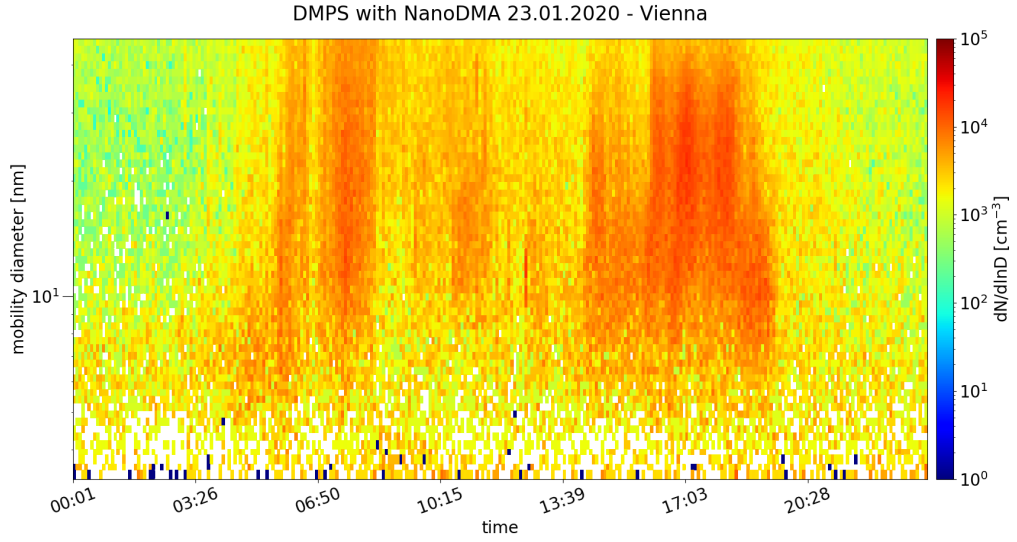

Figure 4.5: Exemplary time evaluation of the PSD measured by the NanoDMPS.

To combine these two ac PSDs to one distribution, with a mobility diameter size range from 2.97 nm to 931.80 nm, it is necessary to average the particle number concentration of the mobility diameters, which was measured by the NanoDMPS in the period of one run of the LongDMPS.

4.3 Uncertainties

The uncertainties of the calibration data, the total concentration, and the averaged concentration of the NanoDMPS were calculated by using the mean values and the standard deviations.
The uncertainties of the concentrations measured by the LongDMPS are the uncertainties of the used instruments shown in Table 4.3.

instrument	uncertainty	[%]
CPC TSI 3776	particle number concentration	10.0
Flowmeter TSI Series 4100	flow rate	2.0

Table 4.3: Uncertainties of the used instruments [44], [40].

The uncertainties of the mobility diameters are calculated using the DMA resolution R

$$R = \frac{Q_{sample} + Q_{sample_{ex}}}{Q_{sh} + Q_{sh_{ex}}} \tag{4.1}$$

[38].

Chapter 5

Results

5.1 Rooftop measurements of the Vienna Urban Aerosol

5.1.1 Total concentration

In Figure 5.1, the weekly cycle of the total concentration, measured with the reference CPC, is shown. A variation of the concentrations can be observed for each weekday. On most days, higher concentrations occur during the morning rush hours (6 am to 8 am), during lunchtime (11 am to 01 pm), and in the evening rush hours (5 pm to 7 pm). On Sunday, it can be observed, that the concentrations, compared to the other weekdays, are lower throughout the day.
As seen in Table 5.1, the highest concentrations are occurring during the morning rush hours, from Monday to Saturday, which are between 17821.50 cm^{-3} and 11559.23 cm^{-3}. On Sunday, a peak during the morning rush hours can not be observed. A second peak can be identified during the lunchtime from Monday to Sunday. Here the concentrations fluctuate between 9727.97 cm^{-3} and 16027.69 cm^{-3}. Additionally, a peak during the evening rush hour can be observed during the whole week. Here the highest values are between 11035.18 cm^{-3} and 25981.64 cm^{-3}. Even though peaks can be identified on Sunday during the evening rush hours and lunch time, the concentrations are generally lower compared to the other days.

	morning rush hours [cm^{-3}]	lunchtime rush hours [cm^{-3}]	evening rush hours [cm^{-3}]
Monday	11559.23 $\pm$ 2568.65	12348.24 $\pm$ 3538.99	11552.28 $\pm$ 689.50
Tuesday	17821.50 $\pm$ 9064.38	11119.30 $\pm$ 4826.74	12957.51 $\pm$ 5826.46
Wednesday	13989.96 $\pm$ 11780.03	11388.50 $\pm$ 5620.31	11035.18 $\pm$ 2292.85
Thursday	17414.26 $\pm$ 6290.17	16027.69 $\pm$ 5631.25	25981.64 $\pm$ 10917.60
Friday	12899.03 $\pm$ 5659.28	11418.33 $\pm$ 1195.50	11585.97 $\pm$ 3791.30
Saturday	12895.45 $\pm$ 10384.12	11776.37 $\pm$ 3388.38	16247.49 $\pm$ 8329.64
Sunday	6948.55 $\pm$ 4956.25	9727.97 $\pm$ 2757.66	11432.86$\pm$ 4564.76

Table 5.1: Highest peak value during the rush hours measured with the reference CPC.

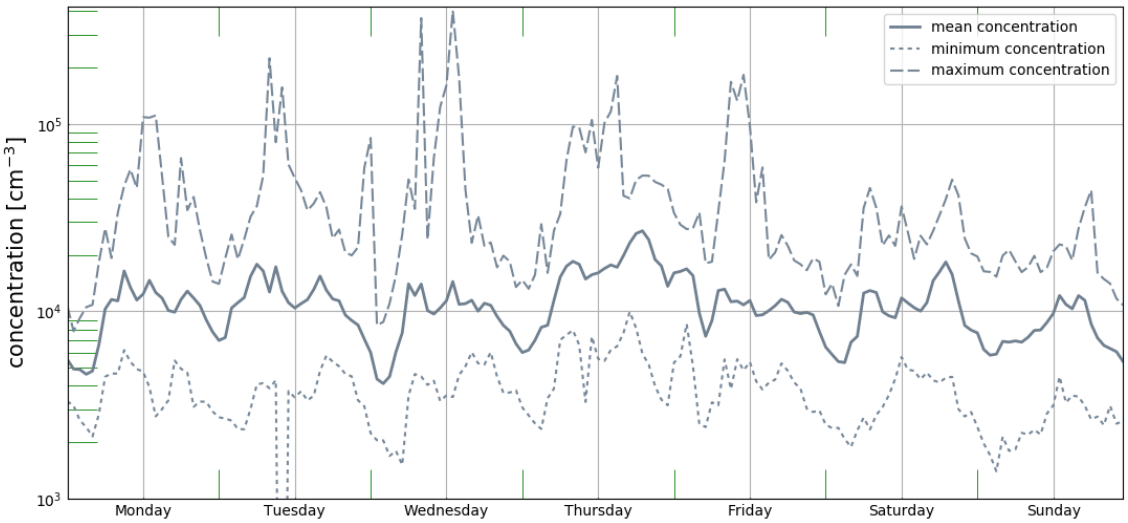

Figure 5.1: Weekly cycle of the total concentration, measured with the reference CPC. The gray line represents the mean concentration, the dashed gray line represents the maximum- and the dotted gray line the minimum- value of each hour.

In Figure 5.2, the weekly cycle of the total concentration measured with the scanning mobility particle sizer (SMPS) is shown. It can be seen that the lowest concentrations occur on Sunday. Additionally, the same structure of a daily cycle can be seen compared to the weekly cycle measured with the reference CPC. A rise of concentrations can be observed two to three times a day.

During the morning rush hours, on the workdays (Monday to Friday), the highest concentrations fluctuate here between 3001.44 cm^{-3} and 7997.11 cm^{-3}. The concentrations rise a second time each day during lunch time. During the workdays the particle number concentration fluctuate between 2682.14 cm^{-3} and 6240.89 cm^{-3}. The last rise of the concentrations is during the evening rush hours. The concentrations fluctuate during the whole week between 4433.51 cm^{-3} and 11433.89 cm^{-3}. The day with the lowest concentrations is again Sunday.

	morning rush hours [cm^{-3}]	lunchtime rush hours [cm^{-3}]	evening rush hours [cm^{-3}]
Monday	3001.44 ± 947.24	4456.34 ± 1558.99	4618.78 ± 2042.74
Tuesday	7997.11 ± 3674.96	5838.43 ± 4000.79	5729.23 ± 4204.20
Wednesday	3542.78 ± 2289.28	2682.14 ± 1004.20	3934.19 ± 1295.85
Thursday	5365.52 ± 2698.94	6240.89 ± 4226.47	11433.89 ± 4400.76
Friday	4944.46 ± 3546.28	4223.23 ± 1258.50	4433.51 ± 557.90
Saturday	4478.91 ± 2573.83	3981.97 ± 1509.75	8548.28 ± 5102.17
Sunday	1951.75 ± 934.45	2850.61 ± 623.54	5158.04 ± 3347.28

Table 5.2: Highest peak value during the rush hours measured with SMPS

The total particle number concentrations of the weekly cycle are shown in Figure 5.3. The grey curve represents the concentrations measured with the reference CPC and the pink curve represents the particle number concentration measured with the SMPS. It can be seen very clearly

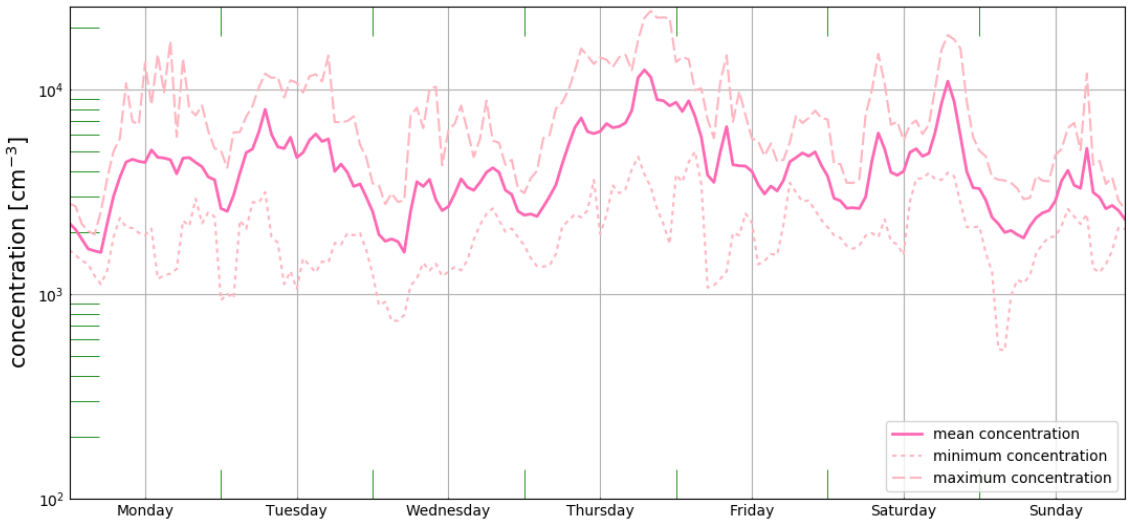

Figure 5.2: Weekly cycle of the total concentration, measured with the SMPS. The pink line represents the mean concentration, the dashed lightpink line represents the maximum- and the dotted lightpink line the minimum- value of each hour.

that the particle number concentrations measured with the reference CPC are higher compared to the particle number concentrations measured with the SMPS. Here the average factor between both mean concentrations is 2.5. The difference between the total concentrations measured with the CPC and the SMPS is probably because both devices have different cut-offs. The CPC cut-off is 2.5 nm, whereas the cut-off of the SMPS is only 7 nm. The structures of both weekly cycles are very similar. The highest values of the particle number concentrations on each day take place at the same time.

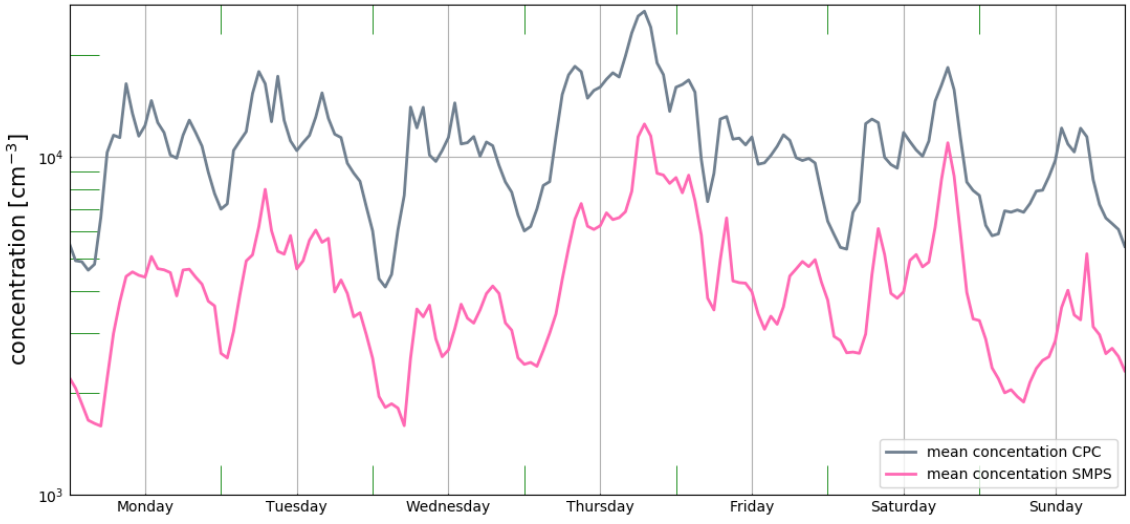

Figure 5.3: Weekly cycle of the total concentration, grey represents the mean particle number concentration measured with the reference CPC and pink represents the mean particle number concentration measured with the SMPS.

5.1.2 Time evolution of the particle size distribution

The time evolution of the PSD was measured by the two parallel DMPS described in section 3.3. To compare these data, a SMPS system from TSI measured the time evaluation of the PSD and the total concentration during the measurement period as well. The mobility diameter selected by the SMPS was in a range from 10.6 nm to 495.8 nm. The mobility diameter selected by the combined DMPS system was in a range from 2.97 nm to 931.80 nm signals of the two DMPS are combined at a mobility diameter of 30 nm. The time resolution of the SMPS system is 5 minutes, and the time resolution of the parallel DMPSs is about 20 minutes. In the following plots, the upper plot represents the time evaluation of the PSD, and the lower plot the total concentration of a specific day. The colours in the upper plot represent the particle number concentrations. Red is an indicator of high concentration and blue for low concentration. The total concentration was calculated by averaging the concentrations during one measurement period of the PSD.

22.01.2020 - 26.01.2020

The measurements during Wednesday, January 22, 2020 are shown in Figure 5.5 and Figure 5.4. In Figure 5.4, a peak with a higher particle number concentration, compared to the rest of the day, can be observed during lunchtime. This peak is located between 5 nm and 30 nm. Also, the accumulation mode can be seen very well.
In Figure 5.5, during lunchtime, a higher particle number concentration compared to the rest of that day, in a range between 13 nm and 200 nm can be observed. Compared to the DMPS, a higher particle number concentration can be seen during the evening and the night. The total concentration measured with the SMPS is lower compared to the total concentration measured with the DMPS.

In Figure 5.6 and Figure 5.7 the measurements during Thursday January 23, 2020 are shown. In Figure 5.6, a peak with higher particle number concentration can be observed in the morning hours. This peak can be separated in two peaks, in the 'first' morning rush hour and in the 'second' morning rush hour. The first peak is located between 5 nm and 40 nm and the second peak between 5 nm and 200 nm. As well as during the evening rush hour, a higher particle number concentration can be recognized between 5 nm and 50 nm. Between 400 nm and 930 nm, the accumulation mode has a lower particle number concentration. During the lunchtime, the particle number concentration is lower compared to the day before (January 22, 2020).
Figure 5.7 has the same structure as the time evolution of the combined DMPSs. Here two peaks during the morning rush hours can be noticed as well. The first peak is located between 10 nm and 200 nm, and the second peak between 10 nm and 300 nm. The SMPS measured a higher particle number concentration during the lunchtime as the time evolution of the combined DMPS and compared with the day before. In the evening, another peak with a higher concentration between 10 nm and 50 nm occurs. This peak is similar to the measurements from the combined DMPS. Most of the day, the total concentrations are higher compared with the day before.

The measurements during Friday January 24, 2020 are shown in Figure 5.8 and Figure 5.9 .

Compared with the days' before, there are lower concentrations during the rush hours, which can be seen in Figure 5.8. A peak between 8 nm and 40 nm can be recognized during nights. Moreover, two peaks during the morning rush hours can be noticed. Those peaks are shorter in time and with fewer particles between 8 nm and 40 nm compared to the other workdays in that week. The second peak can be detected between 10 nm and 40 nm. This peak is shorter in time as well and has less particle number concentration compared to the other workdays. In the evening, the particle number concentration is higher compared to the afternoon. The accumulation mode between 90 nm and 200 nm can be observed the whole day. The accumulation mode between 500 nm and 930 nm can be seen very well.
Compared to the DMPS systems the SMPS shows a higher particle number concentration between 50 nm and 300 nm during the whole day, which can be seen in Figure 5.9.
The peak during the morning rush hours is wider in time compared to the measurements with the combined DMPS system. Here a higher particle number concentration can be observed during the whole afternoon and in the evening in contrast to the time evaluation of the combined DMPS. The accumulation mode between 60 nm and 300 nm can be seen very clearly in Figure 5.9.

The measurements during Saturday January 25, 2020 are shown in Figure 5.10 and Figure 5.11. Compared to the workdays, a lower particle number concentration can be noticed during the whole day. Here the accumulation mode can be identified very clear between 60 nm and 300 nm.

The measurements during Sunday January 26, 2020 are shown in Figure 5.12 and Figure 5.13. Compared to the rest of the week, the particle number concentration on this Sunday is very low. The accumulation mode can be seen clearly between 70 nm and 200 nm in Figure 5.13.

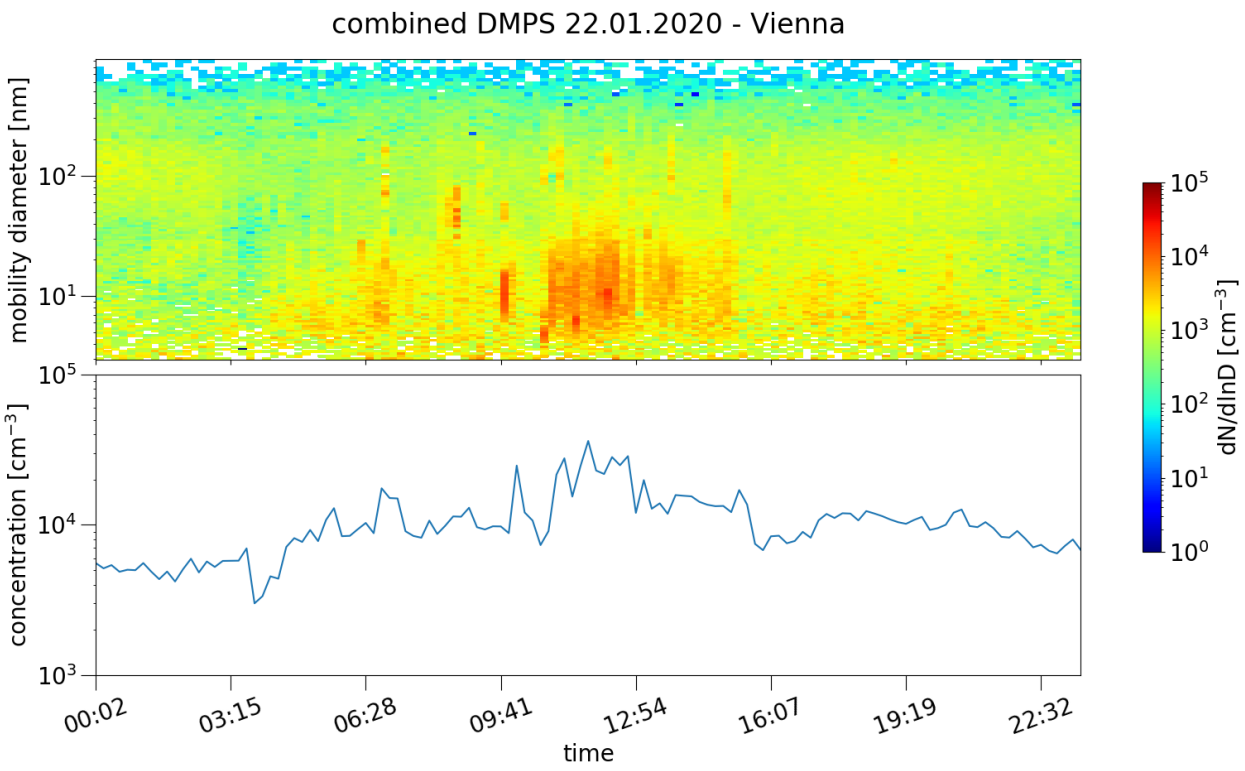

Figure 5.4: DMPS 22.01.2020

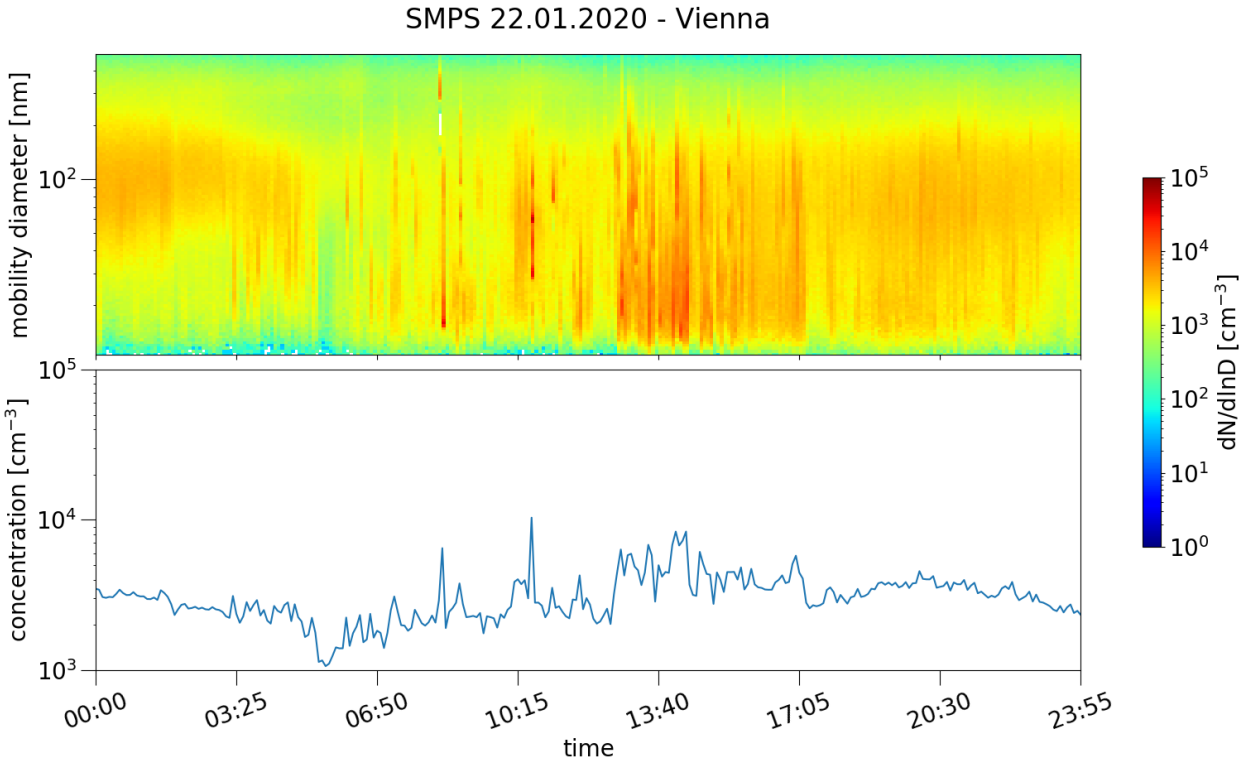

Figure 5.5: SMPS 22.01.2020

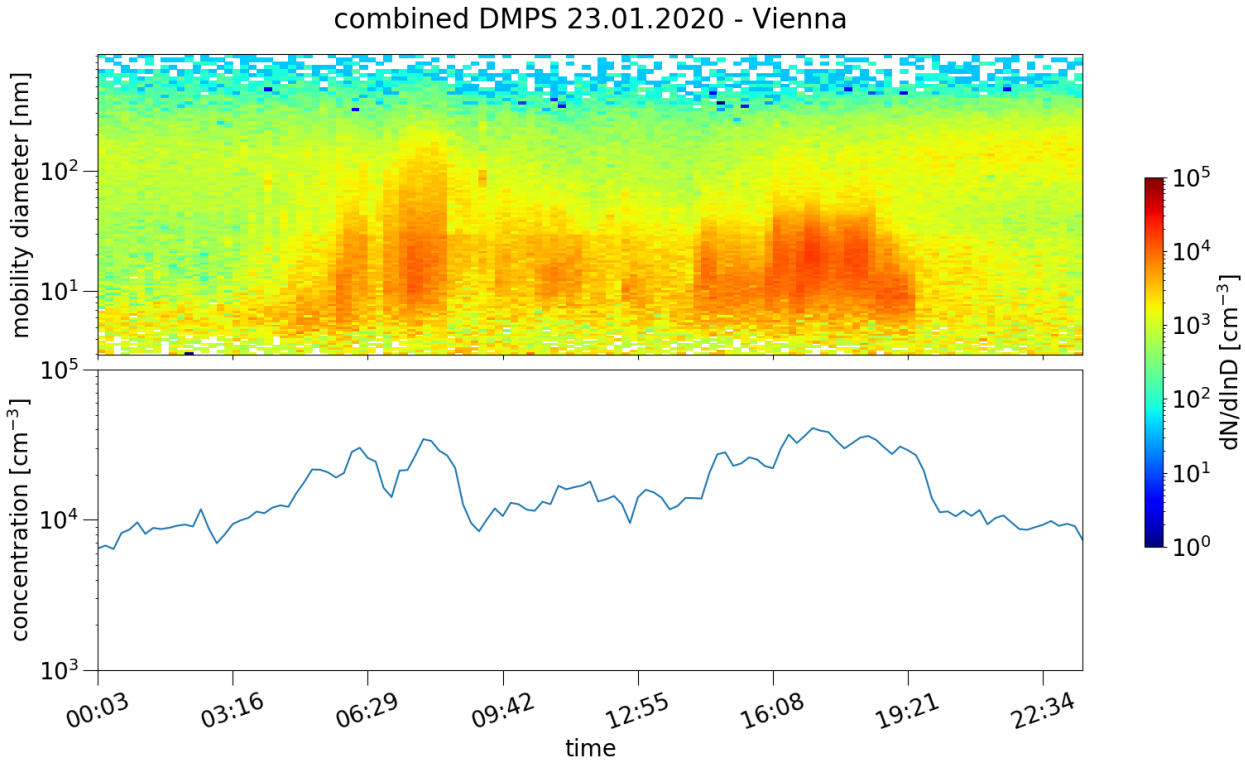

Figure 5.6: DMPS 23.01.2020

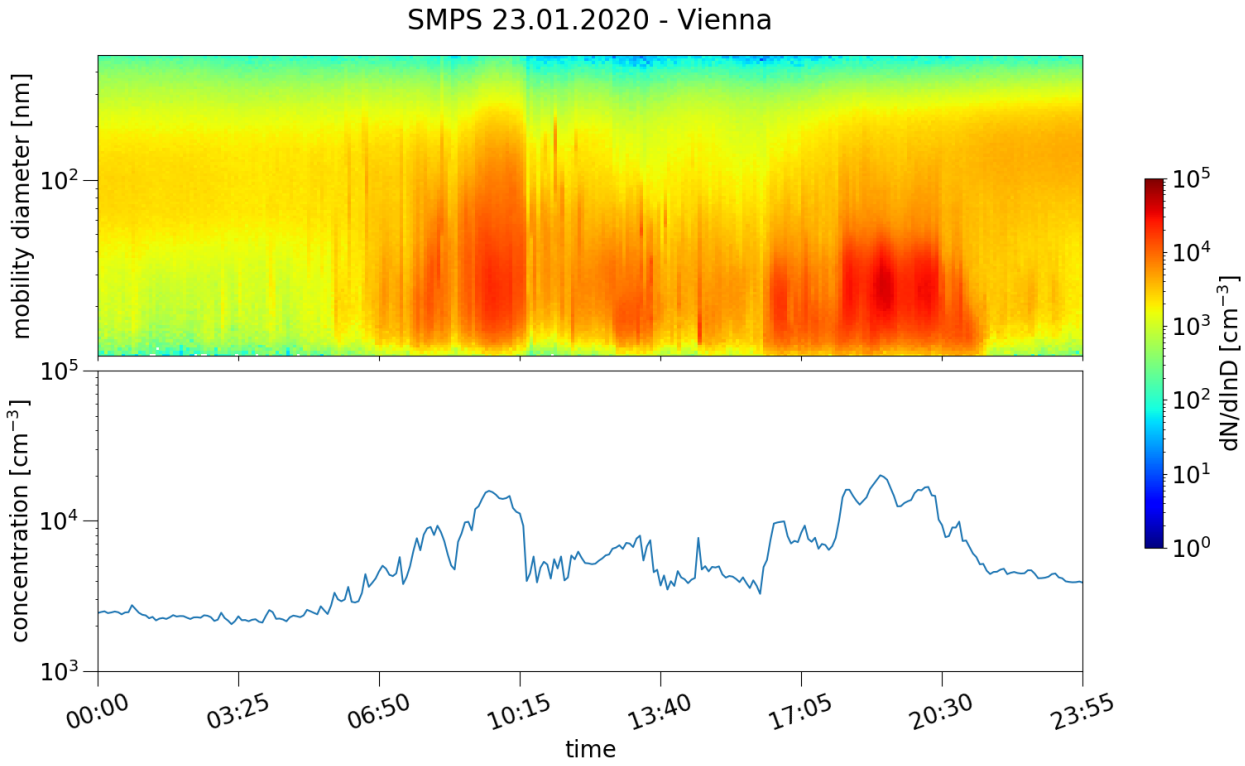

Figure 5.7: SMPS 23.01.2020

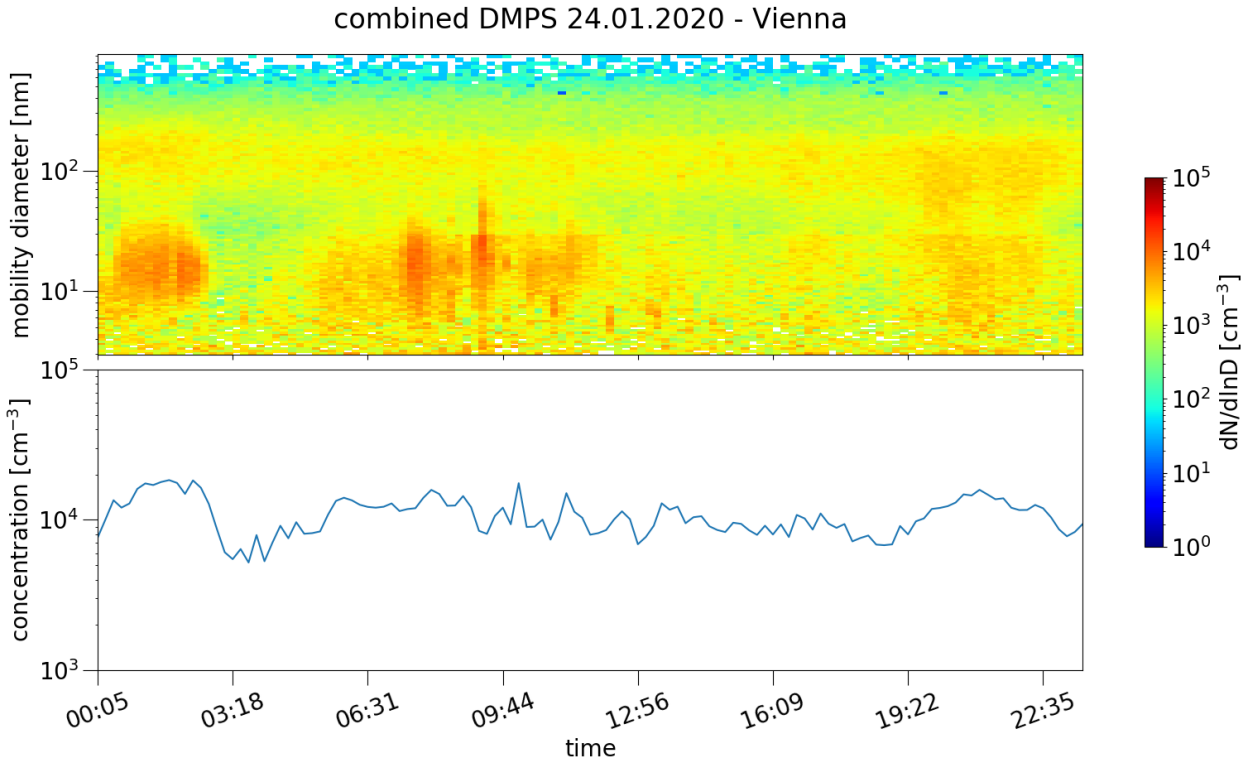

Figure 5.8: DMPS 24.01.2020

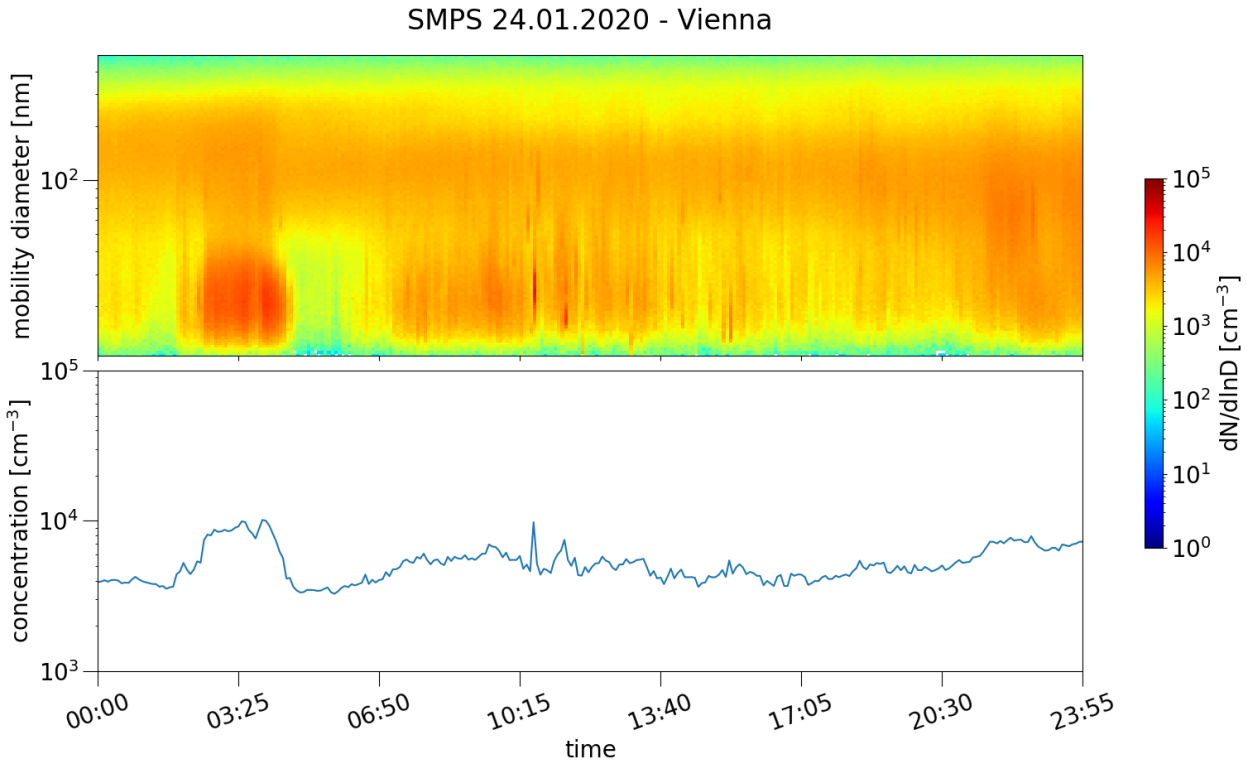

Figure 5.9: SMPS 24.01.2020

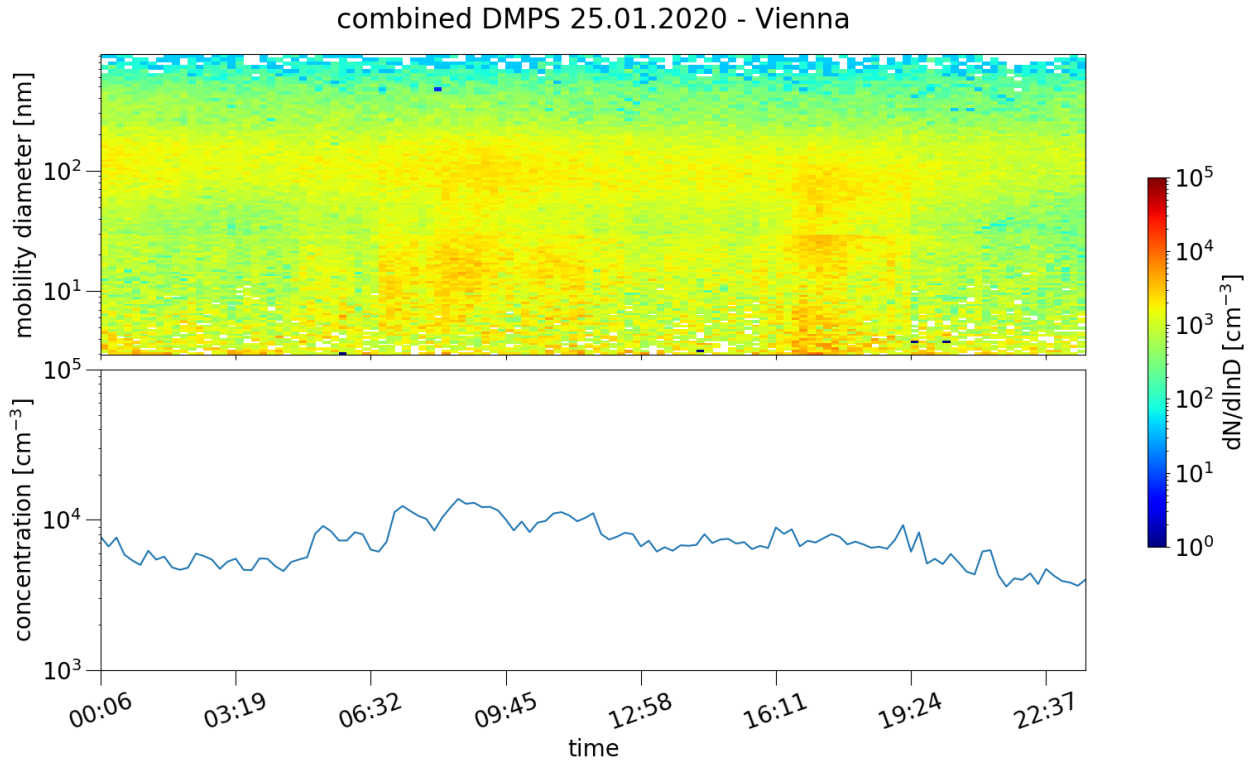

Figure 5.10: DMPS 25.01.2020

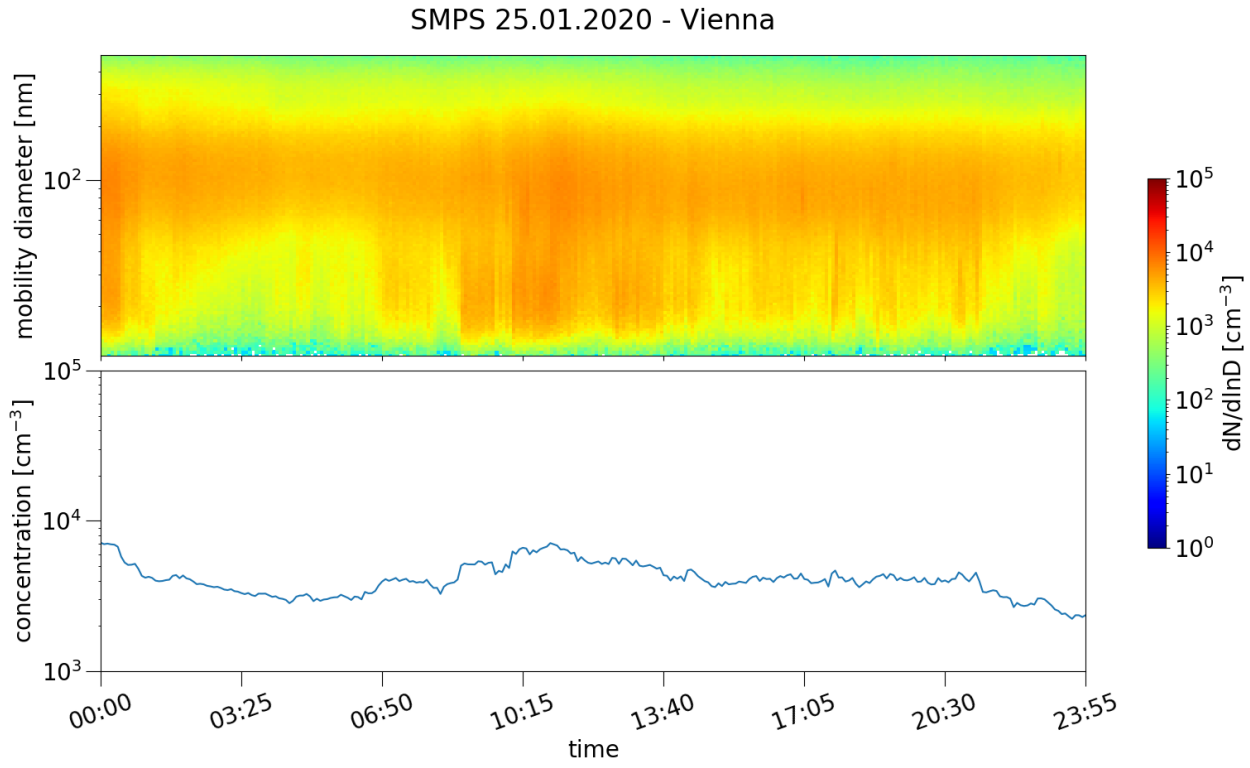

Figure 5.11: SMPS 25.01.2020

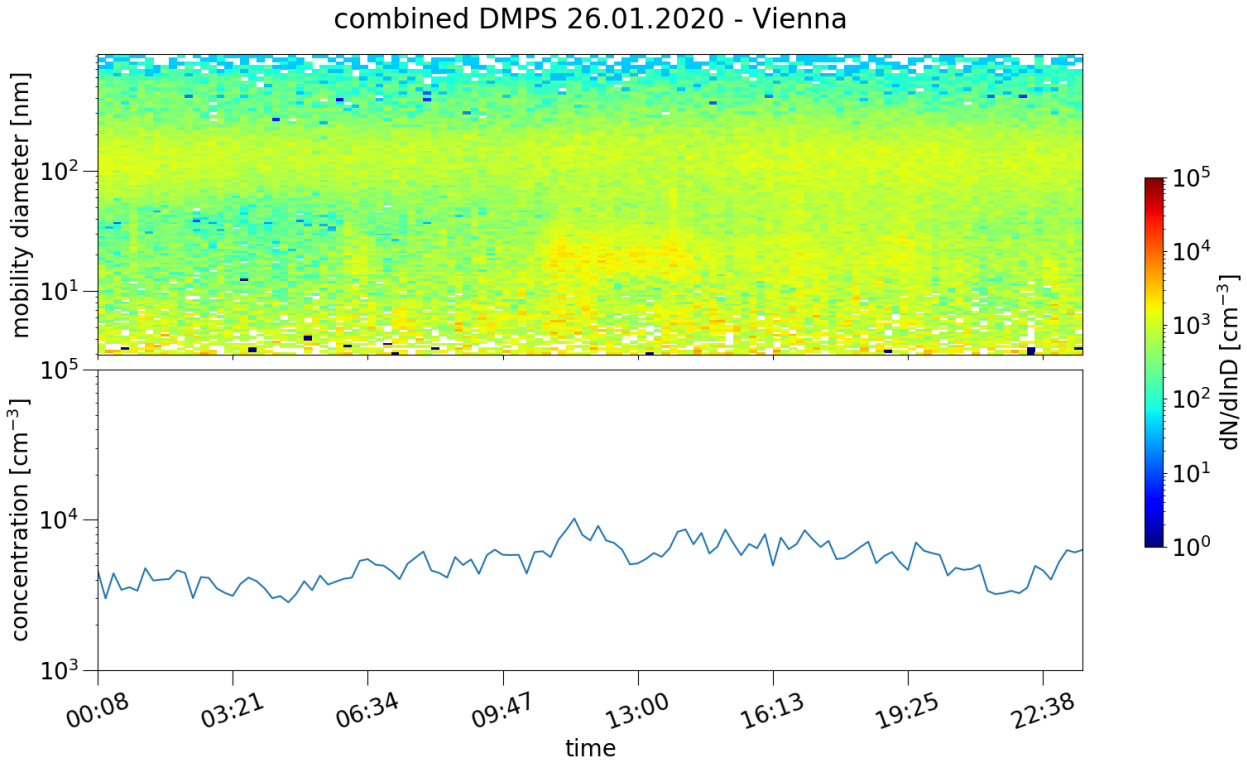

Figure 5.12: DMPS 26.01.2020

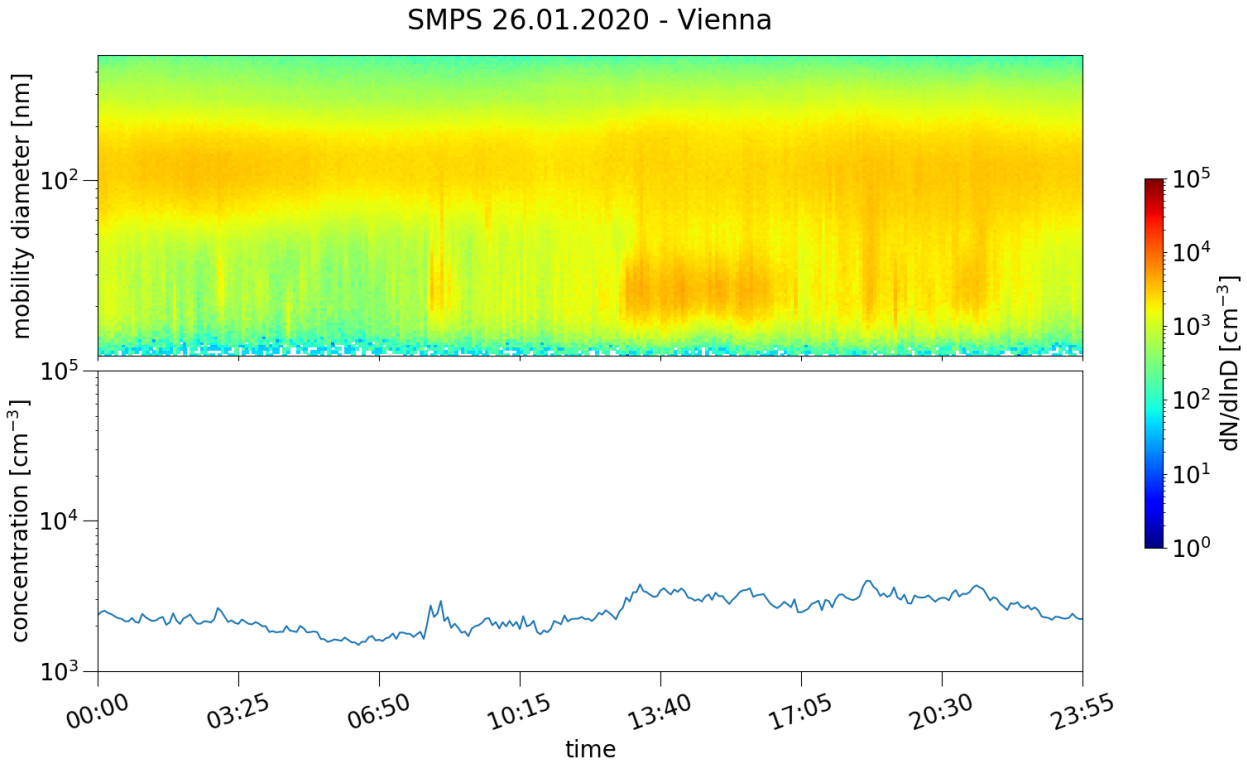

Figure 5.13: SMPS 26.01.2020

27.01.2020 - 02.02.2020

The measurements during Monday January 27, 2020 are shown in Figure 5.14 and Figure 5.15. As can be seen in Figure 5.14, higher particle number concentrations are present during the morning and lunchtime compared to the night. The total concentration raises during the day and falls during nights. As seen in Figure 5.15, the measurements with the SMPS has nearly the same structure compared to the measurements with the combined DMPS. Here the accumulation mode can be identified between 70 nm and 200 nm.

The measurements during Tuesday January 28, 2020 are shown in Figure 5.16 and Figure 5.17. In Figure 5.16, a higher particle number concentration between 5 nm and 200 nm can be observed during lunchtime. Additionally, two peaks were detected during the morning hours. The first is located between 5 nm and 20 nm, and the second between 10 nm and 30 nm. The accumulation mode can be observed from the early morning hours until the afternoon, to a lower limit of 500 nm. A possible reason for this change is a change in the meteorological conditions. In the evening, the particle number concentration falls compared to the rest of that day. In Figure 5.17, the accumulation mode can be seen very clearly in a size range of 70 nm to 200 nm starting from the early morning hours and lasting until the afternoon. This mode can not be observed in the evening whereas the accumulation mode can be seen very clear to a lower limit of 300 nm.

The measurements during Wednesday January 29, 2020 are shown in Figure 5.18 and Figure 5.19. In Figure 5.18 the accumulation mode can not be seen. Here two peaks can be identified during the morning rush hours. The first peak is located between 5 nm and 40 nm and the second peak later between 8 nm and 50 nm. A smaller peak can be seen during the afternoon between 10 nm and 30 nm. Compared to the time evolution of the combined DMPS, the structure of the time evolution measured by the SMPS is very similar, which can be seen in Figure 5.19. In this time evolution of the PSD, two peaks can be found during the morning hours. These peaks are located between 10 nm and 50 nm. A smaller peak can be observed during the afternoon in the same size range, which the combined DMPS detected as well.

The measurements during Thursday January 30, 2020 are shown in Figure 5.20 and Figure 5.21. Compared to the day before, the first peak during the morning rush hour occurs later and has a lower particle number concentration, which is located between 6 nm and 25 nm. The second peak during the morning rush hour is later as well but has a higher particle number concentration between 6 nm and 10 nm compared to the day before. A peak during the lunchtime can be seen very well. The mobility diameter is in a size range from 7 nm to 40 nm. Compared to Thursday January 23, 2020, a higher particle number concentrations, in a size range from 7 nm to 200 nm can be detected, during the afternoon and the evening.

The measurements during Friday January 31, 2020 are shown in Figure 5.22 and Figure 5.23. As seen in Figure 5.24, the structure starts with the same structure as the previous day ended. Before the morning rush hours, this specific structure ended, and the total concentration dropped down. Compared to the days before and to Friday, January 24, 2020, the morning rush hour

does not have that high particle number concentrations. The particle number concentrations are only getting higher between 7 nm and 40 nm during the evening. Here the accumulation can be detected to a lower limit of 300 nm. Compared to the measurements by the SMPS system, the time evolution of the PSD measured by the DMPS system observes a higher particle number concentration during the evening.

The measurements during Saturday February 01, 2020 are shown in Figure 5.24 and Figure 5.25. As seen in Figure 5.24, the accumulation mode can be observed to a lower limit of nearly 200 nm. A peak with high particle number concentration between 6 nm and 80 nm can be detected during the morning rush hours. Compared to the workdays of that week, only one peak can be identified during the morning rush hours. A peak during lunchtime can be located but with lower particle number concentrations and a smaller size range compared to the morning peak. Here is the size range between 8 nm and 40 nm. The peak with the biggest size range of that day occurs during the evening. The mobility diameter is in a size range between 8 nm and 20 nm. In Figure 5.25, during the early morning, an additional structure can be seen compared to the measurement by the combined DMPS. The nuclei mode can be identified very clear between 12 nm and 50 nm.

The measurements during Sunday February 02, 2020 are shown in Figure 5.26 and Figure 5.27. Compared to the day before, only two peaks with a higher particle number concentration can be observed, and these peaks are very close to each other. During lunchtime, the first peak has a mobility diameter range from 6 nm to 20 nm. During the early afternoon, the second peak is located in a size range from 6 nm to 50 nm. The accumulation mode can be observed to a lower limit of 300 nm. Compared to Sunday January 26, 2020, a higher total concentration can be observed, during the day.

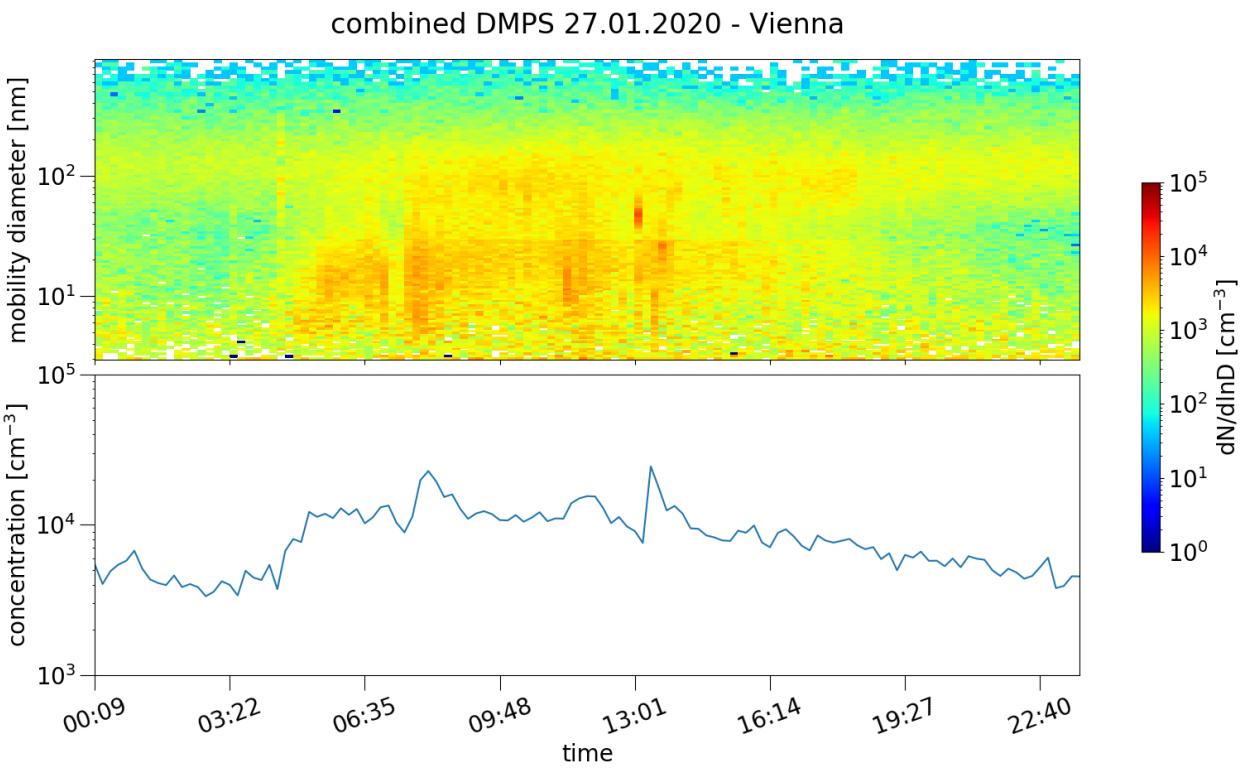

Figure 5.14: DMPS 27.01.2020

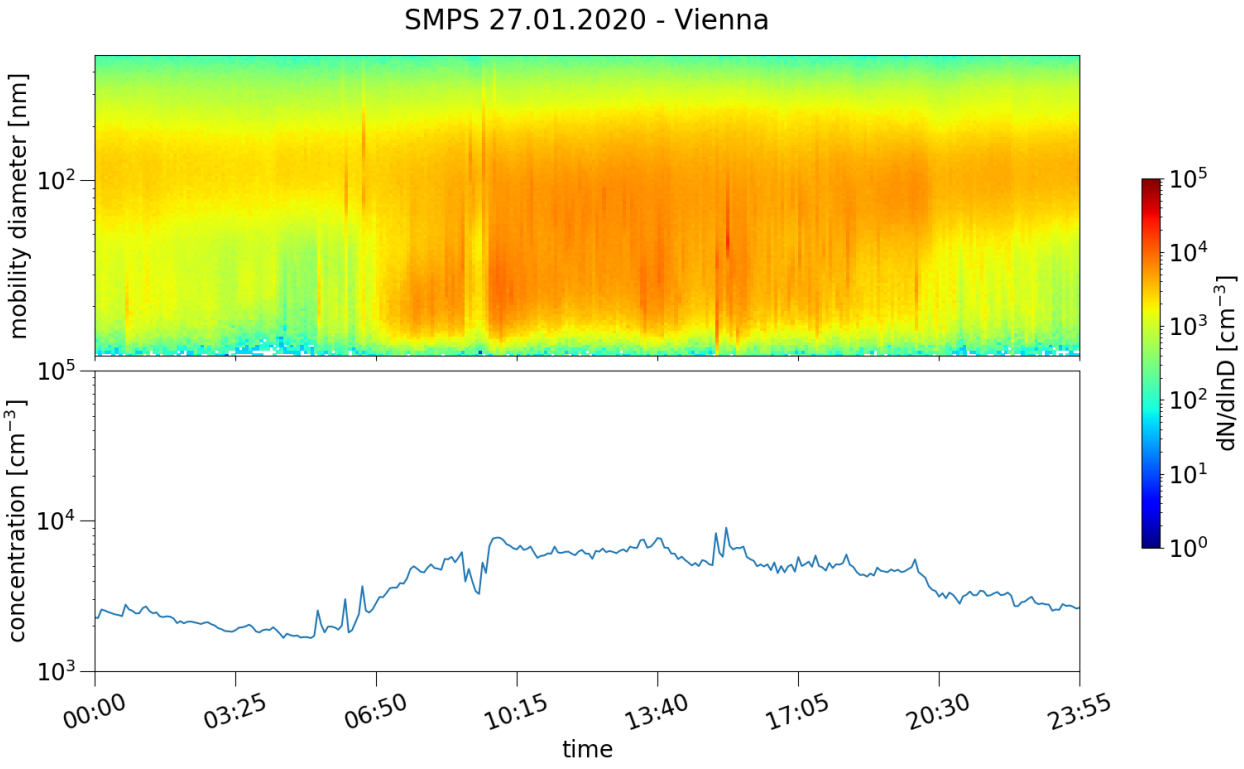

Figure 5.15: SMPS 27.01.2020

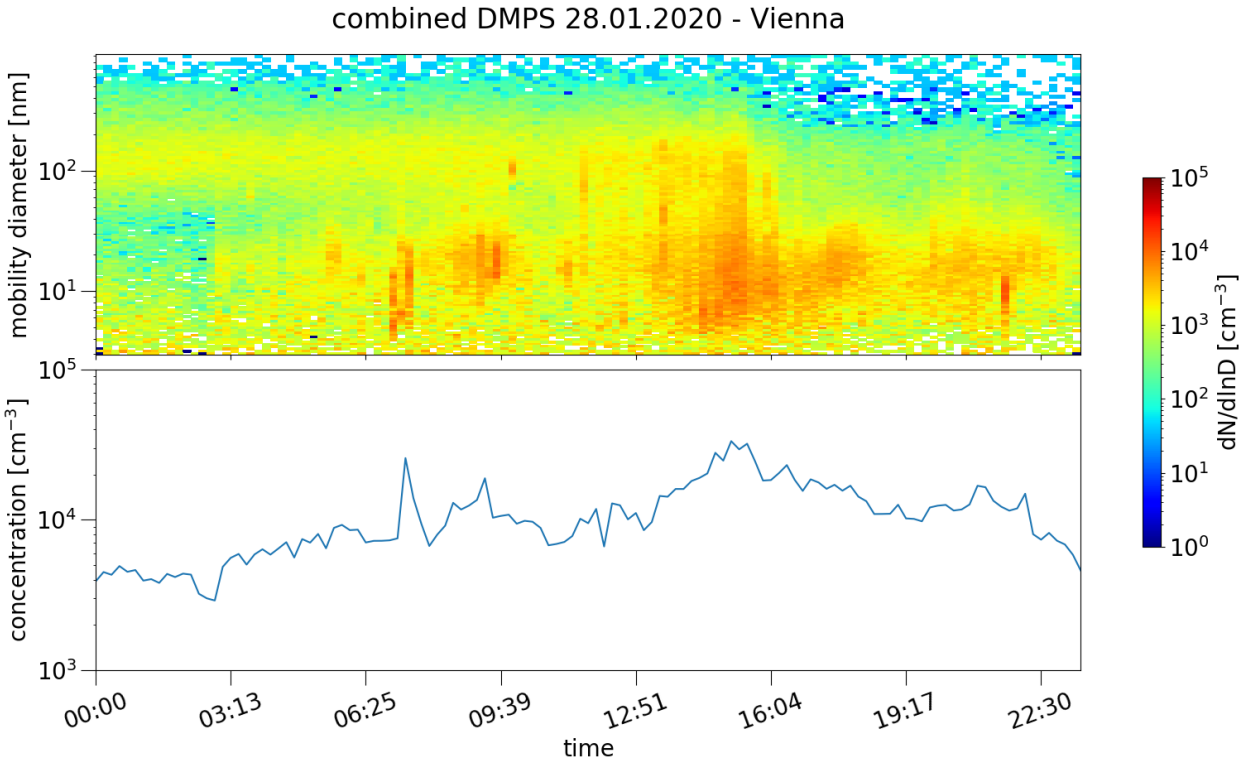

Figure 5.16: DMPS 28.01.2020

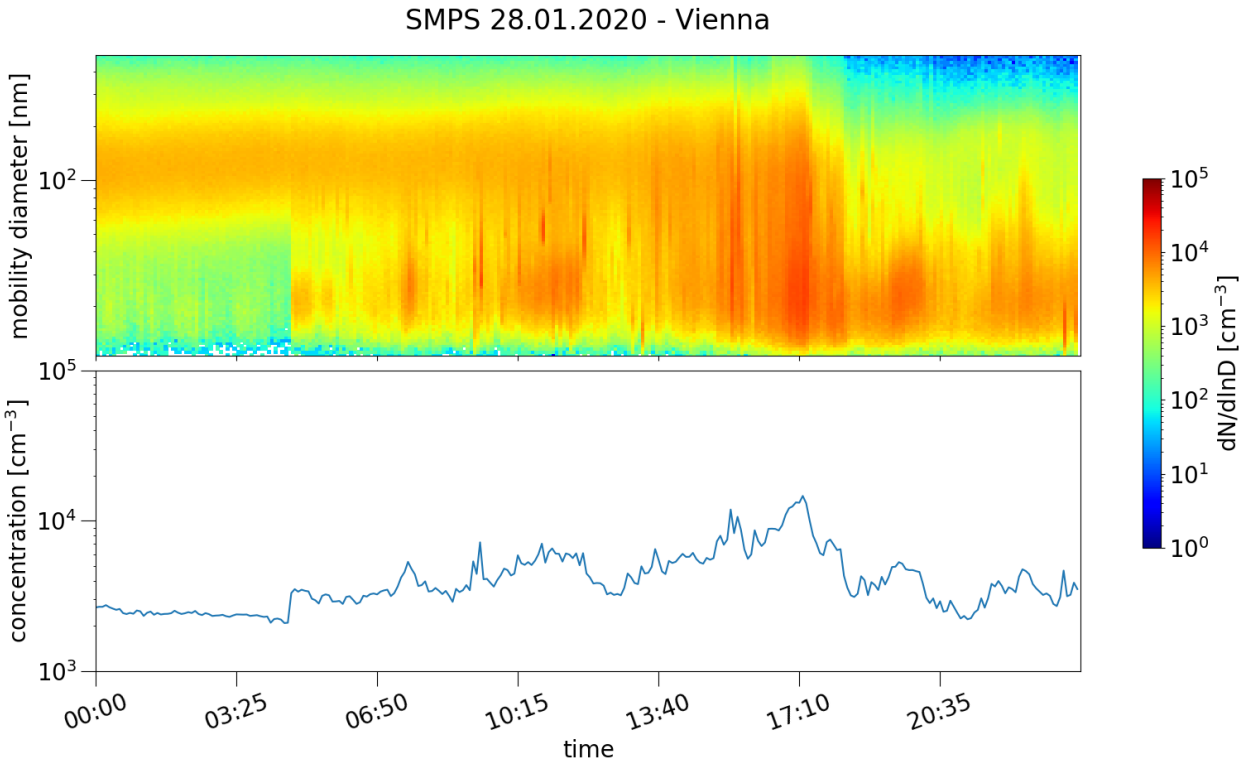

Figure 5.17: SMPS 28.01.2020

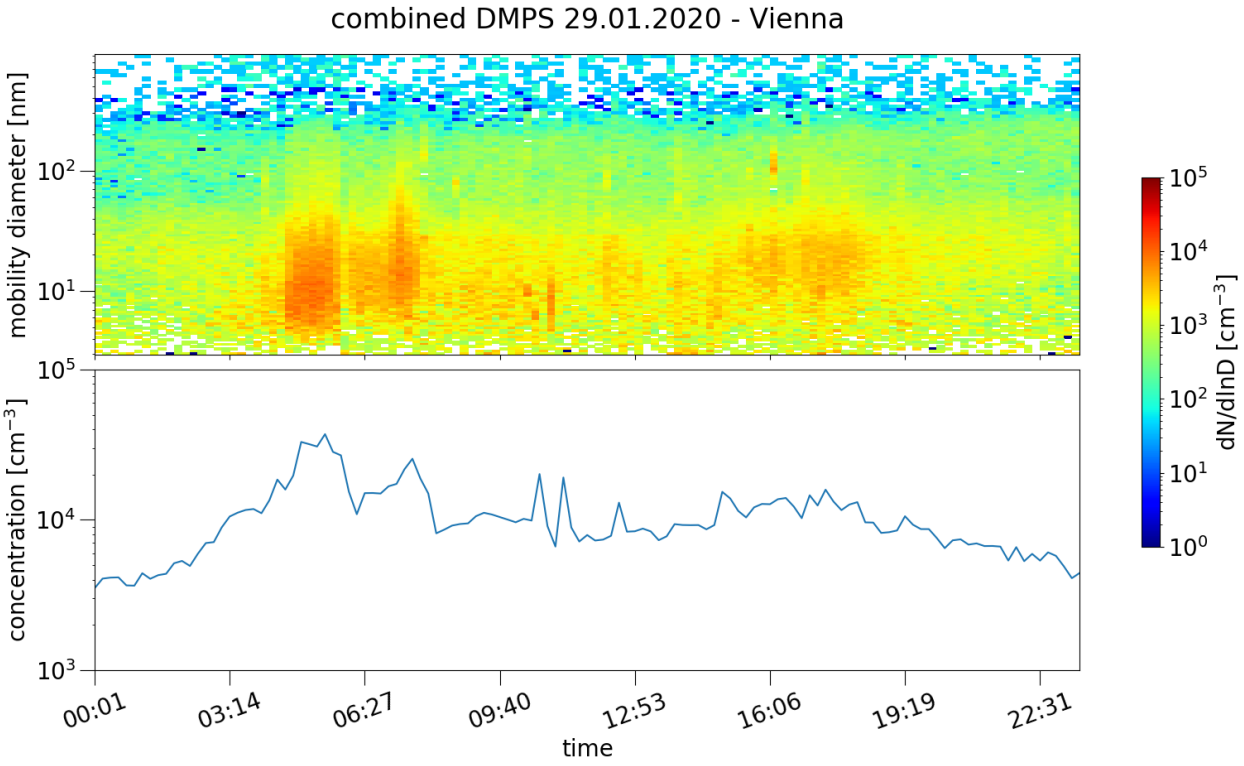

Figure 5.18: DMPS 29.01.2020

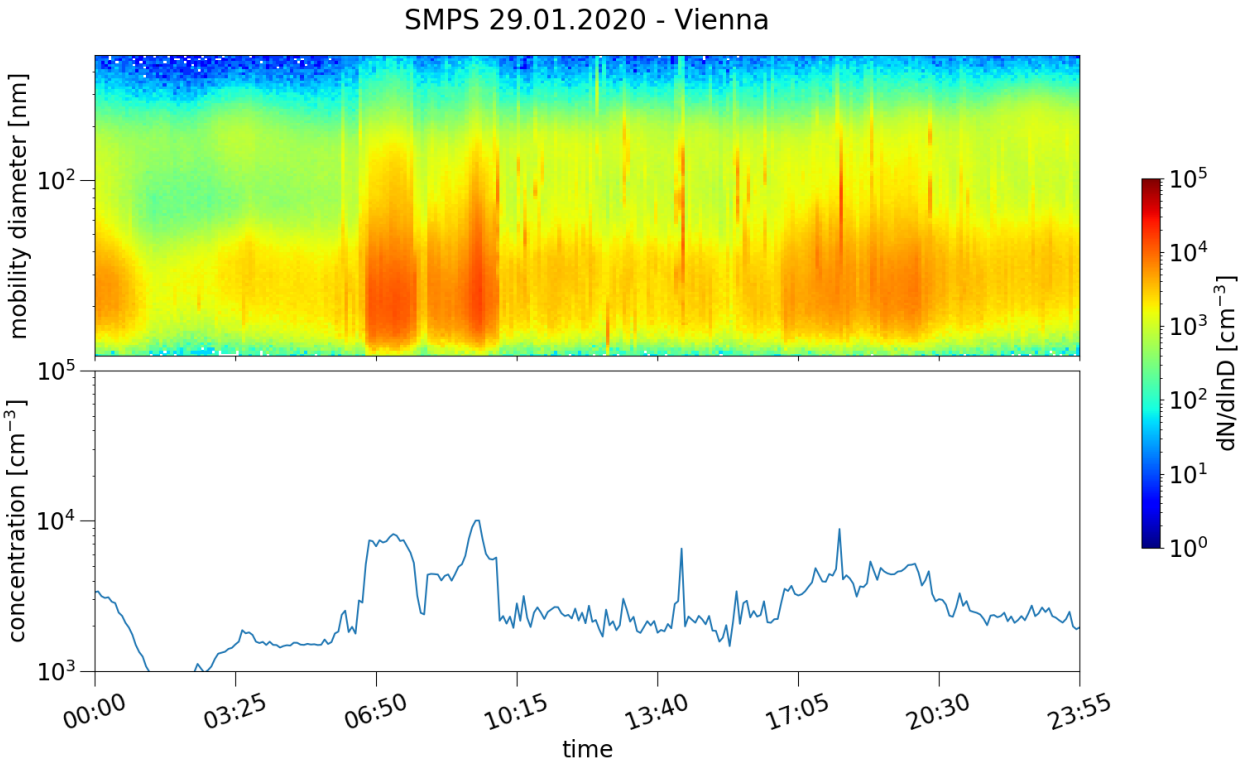

Figure 5.19: SMPS 29.01.2020

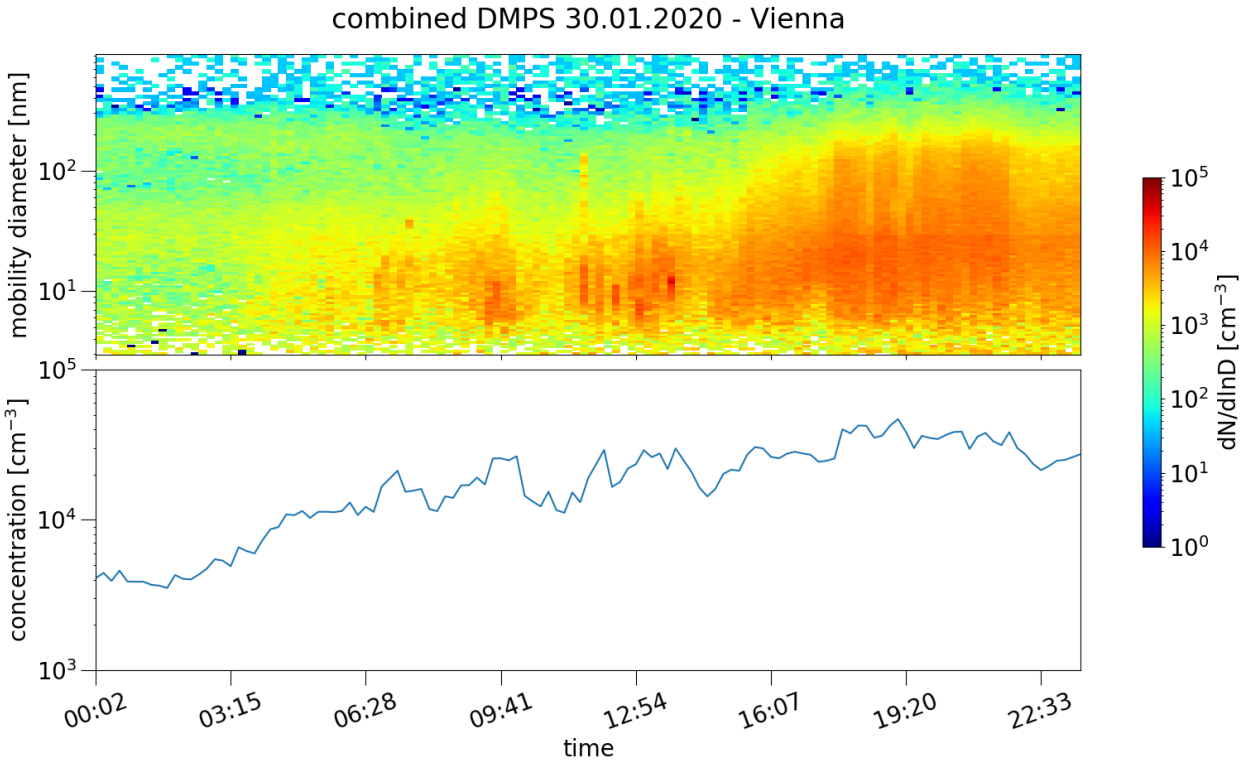

Figure 5.20: DMPS 30.01.2020

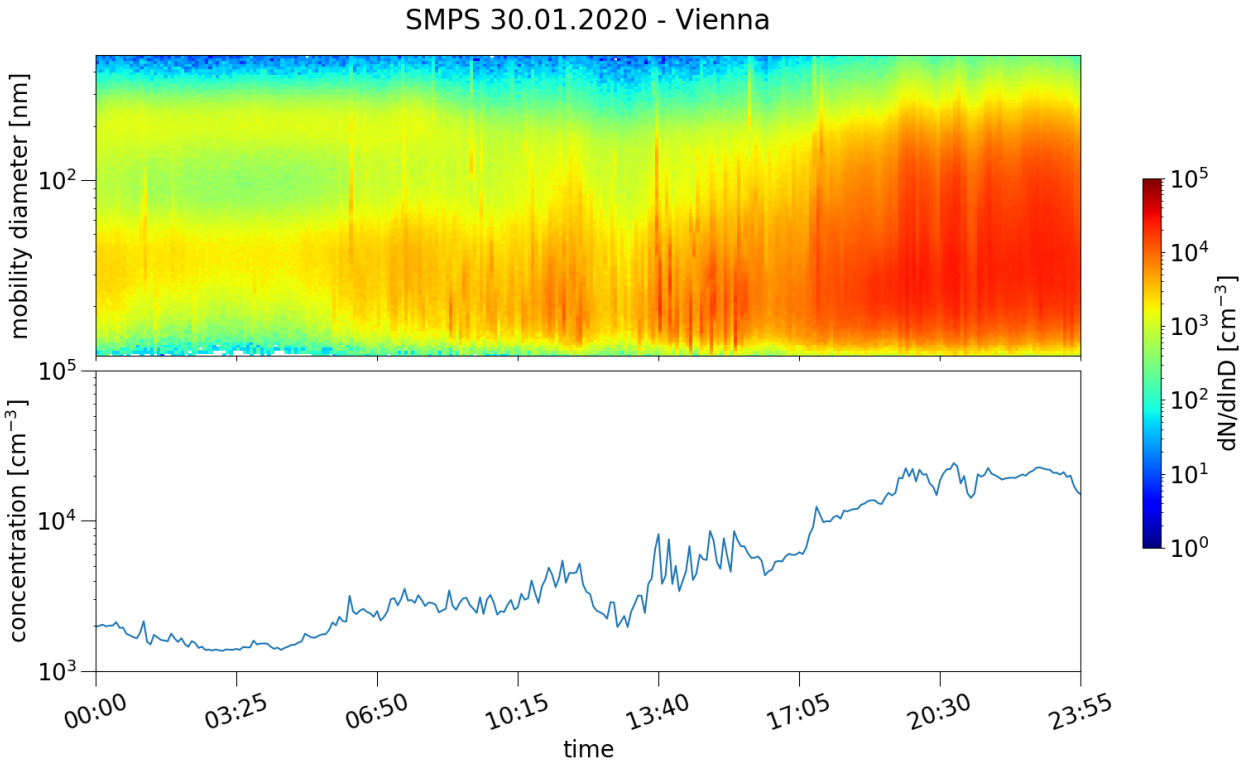

Figure 5.21: SMPS 30.01.2020

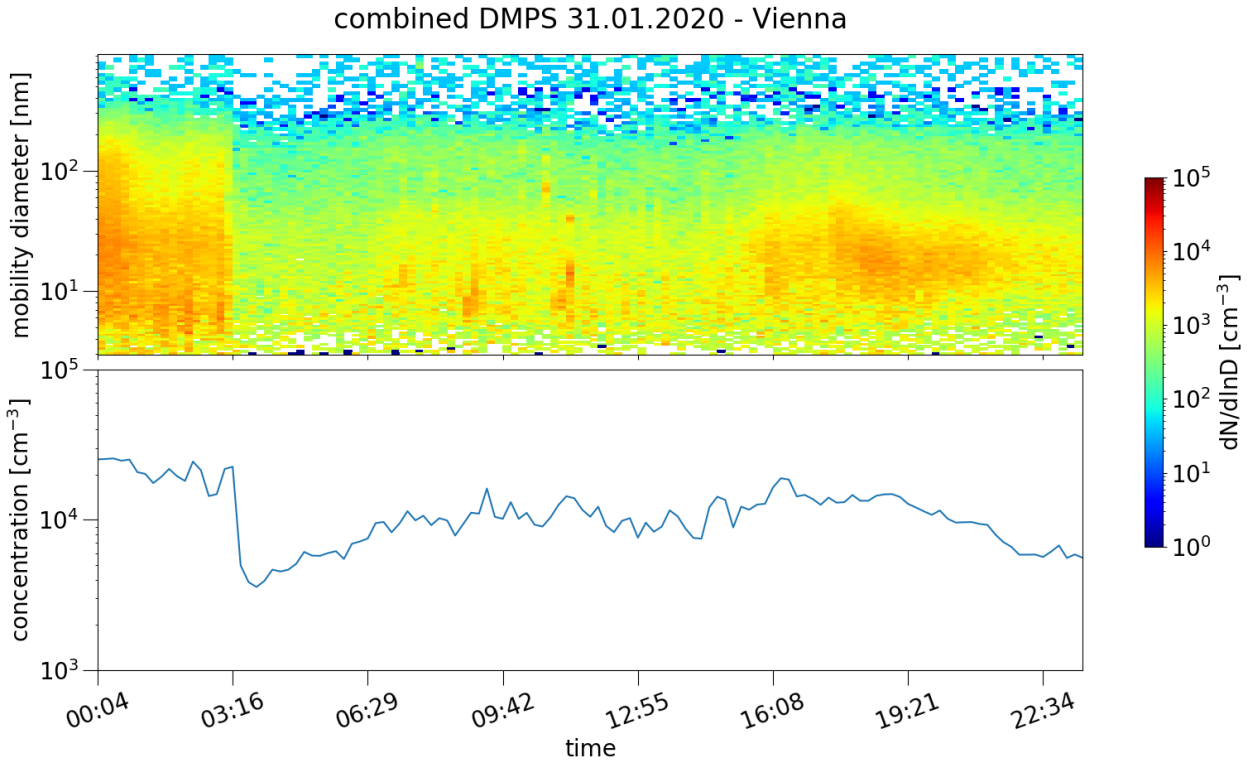

Figure 5.22: DMPS 31.01.2020

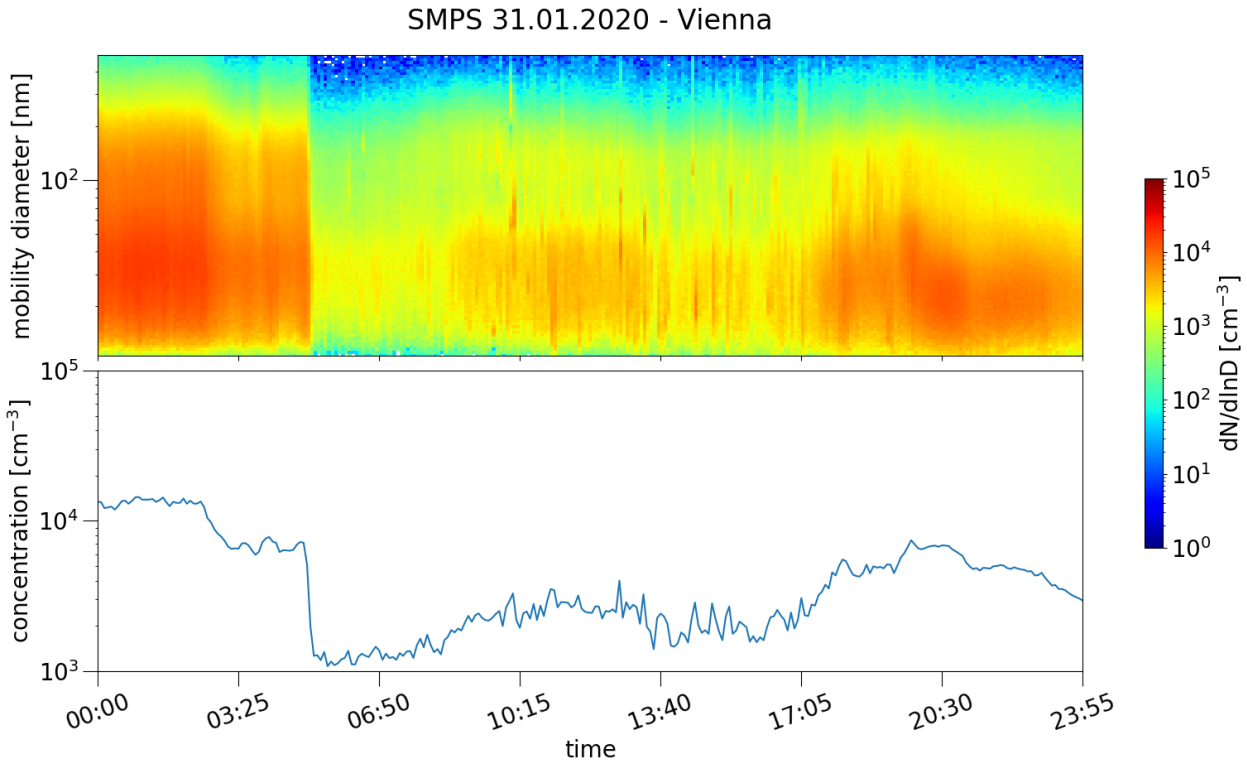

Figure 5.23: SMPS 31.01.2020

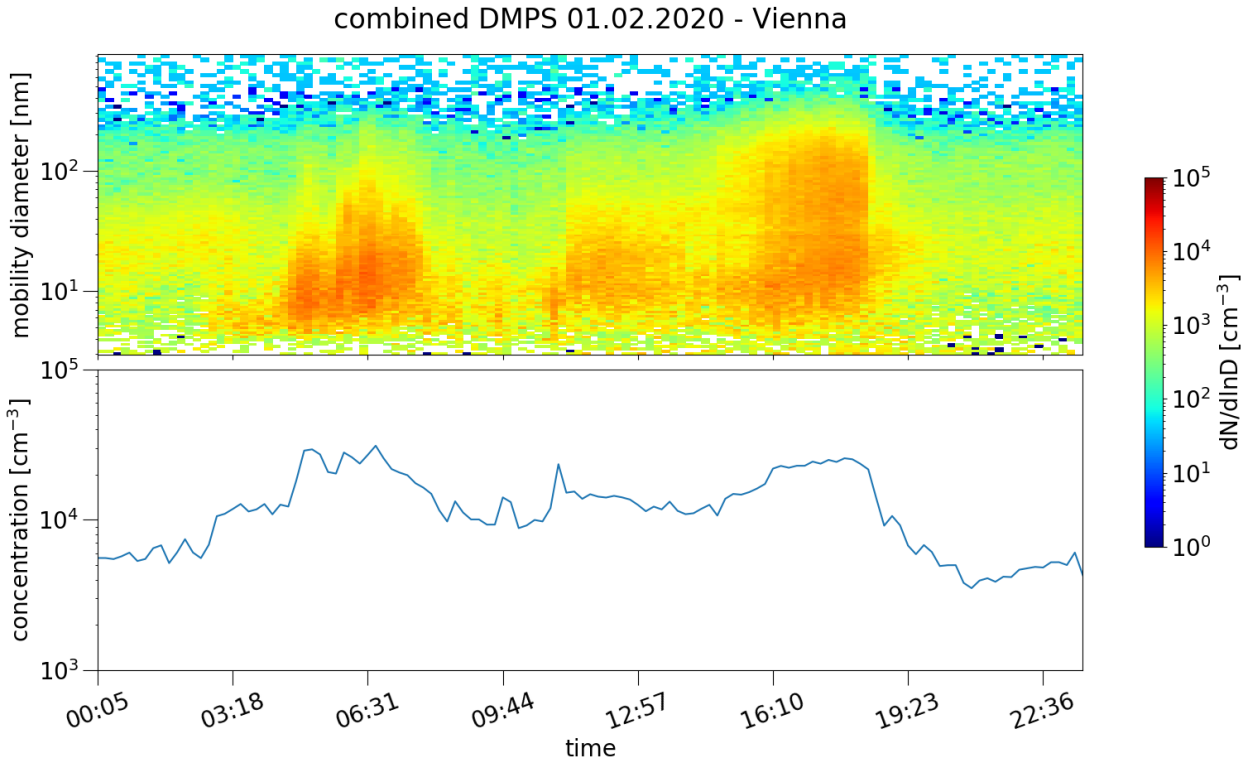

Figure 5.24: DMPS 01.02.2020

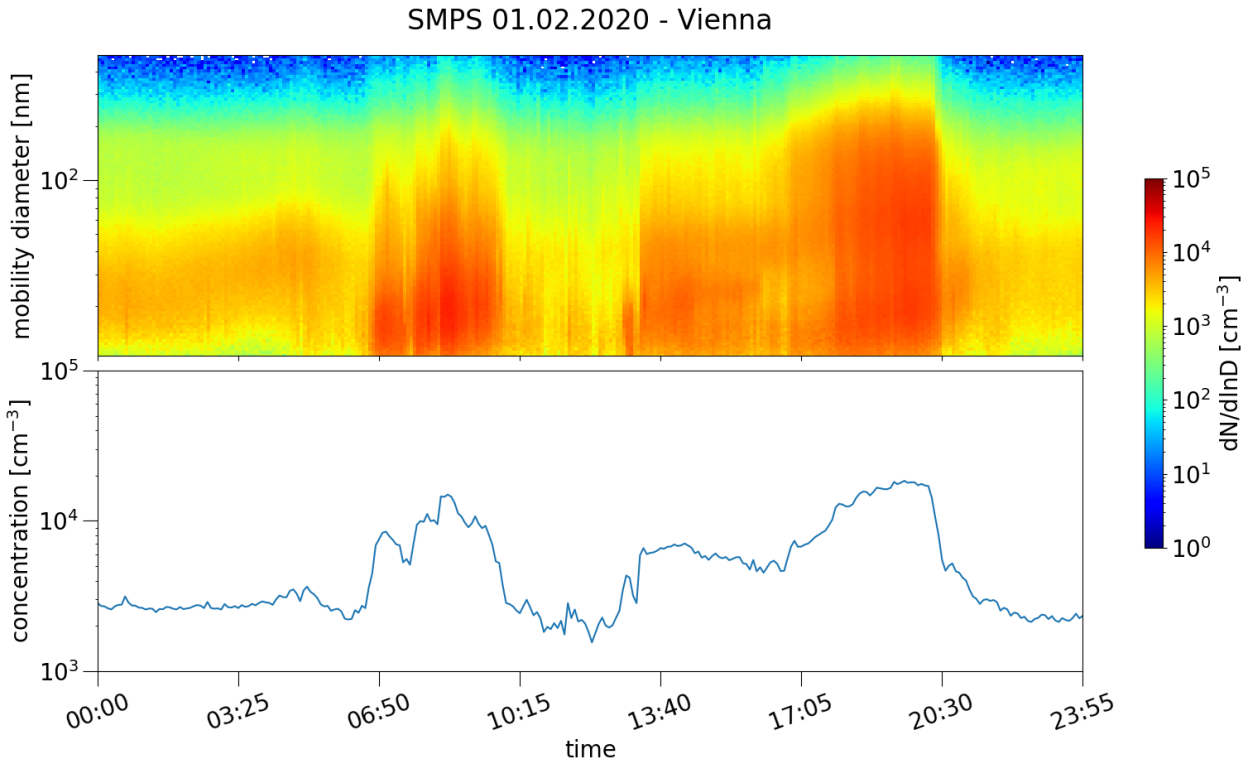

Figure 5.25: SMPS 01.02.2020

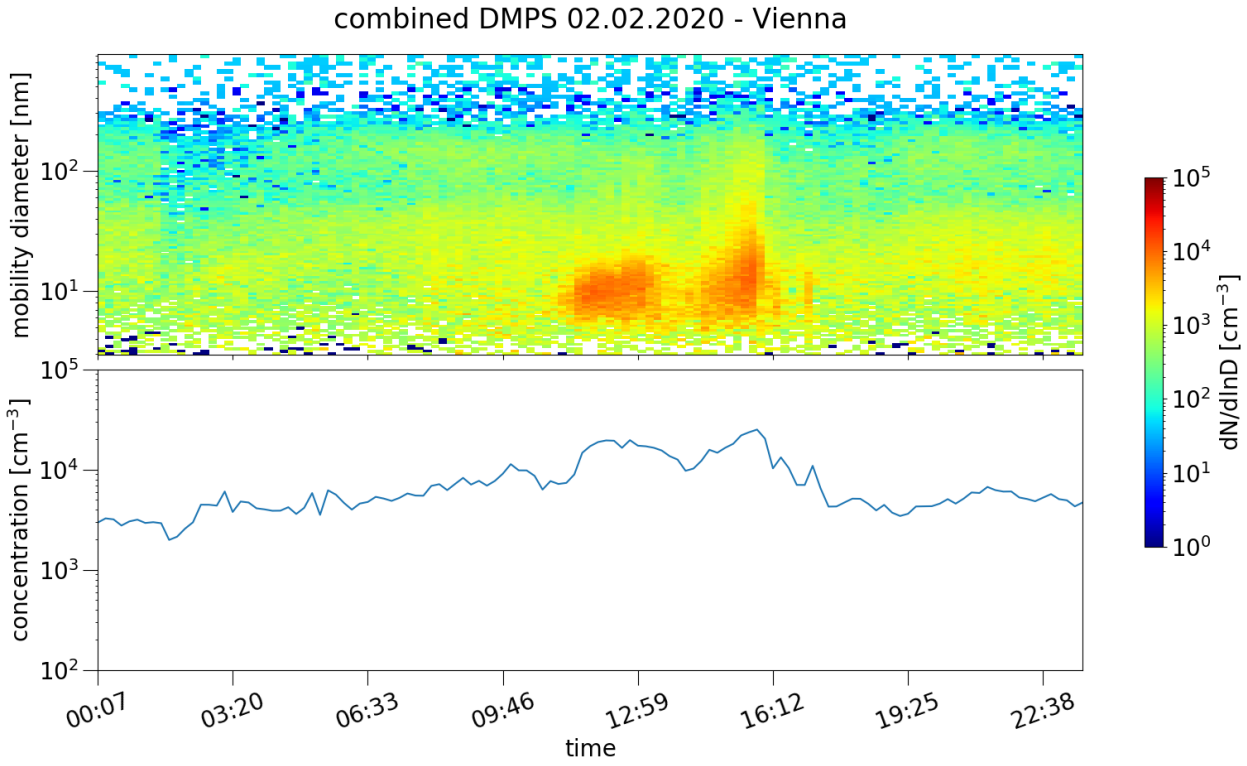

Figure 5.26: DMPS 02.02.2020

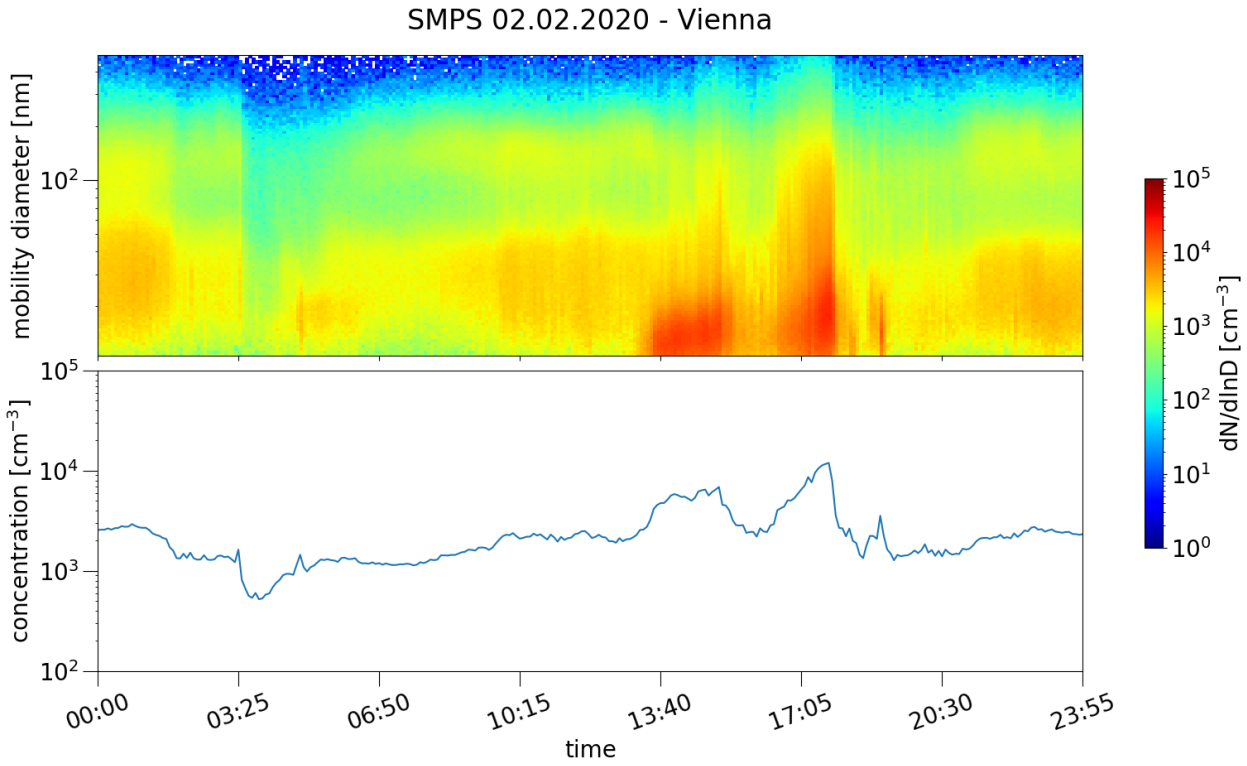

Figure 5.27: SMPS 02.02.2020

Interpetation

During the most working days, a structure that looks like a watermelon, can be observed. During the most days, this structure has a particle mobility diameter between 5 nm and 40 nm. An essential characteristic of the watermelon-structure is that no particle growth can be observed. The particles are all emitted ones, mostly from cars. These structures can occur during the whole day. Most of these watermelons can be detected during rush hour times. An example for a watermelon, during the morning rush hour, can be seen in Figure 5.18, and a model for a watermelon, during the evening rush hour can be seen in Figure 5.6. These watermelons probably observed because of the emitted ultrafine particles from the traffic.
On Thursday January 30, 2020, started at around 05 pm a structure marked with high concentration over the whole particle size range, seen in Figure 5.20,Figure 5.22. This structure ends abruptly on Friday January 31, 2020 around 04 am. The reason for this abrupt end could be a change in the wind direction.

Comparing the commercial SMPS with the home-built DMPS shows an improvement in the size resolution in the sub-10 nm size range because, with the commercial system, it is not possible to measure the particle number concentration under 10 nm. However, the time resolution is better with the commercial SMPS because the time resolution of the SMPS is 5 min and the time resolution of the home-build DMPS is about 20 min.

Classification

The measurement period was 16 days from the end of January to February, with 12 days of useful quality data. No $event$ was identified during this period. Nine out of 16 days are identified as $non\ event$ and three days as $undefined$, which can be seen in Figure 5.28. Days defined as $non\ event$ are marked in green, days defined as $undefined$ are blue, and days with poor quality data are marked in grey.
An example of an $non\ event$ day is January 26, 2020. On that day, no growing mode can be identified. An example of an $undefined$ day is February 02, 2020. Several conditions need to be fulfilled for having an $event$. On this specific day, at least one of the conditions was not fulfilled. One condition is that the mobility diameter has to be smaller than 25 nm, which is fulfilled since the size ranges are located between 6 nm and 20 nm. Another condition is that the growth pattern needs to be consistent over several hours. Since on February 02, 2020, the second named condition could not be fulfilled, so the measurement day is identified as $undefined$.

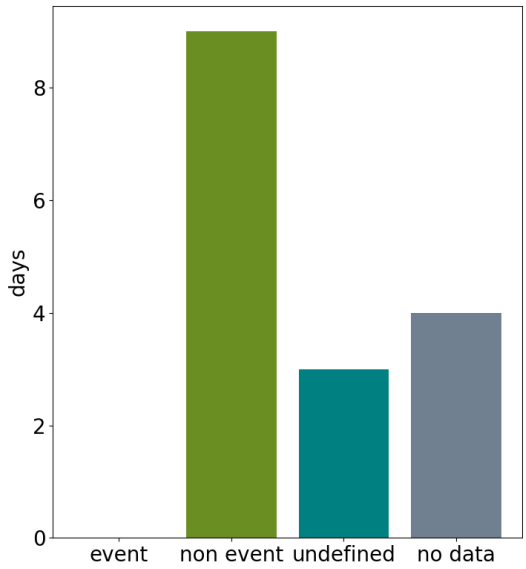

Figure 5.28: Classification of the particle size distribution.

According to [22, 49], the NPF events has a seasonal dependency. During winter, from December to February, the NPF frequency in Vienna, Austria, is lower than six percent of the days. [22] The low NPF frequency during the Winter season could be the reason why no $event$ could be detected during the measurement period. Another possible reason could be the short measurement period.

Chapter 6

Conclusion and Outlook

The aim of this master thesis was to combine two PSD measured with two DMPS systems, which were operated in parallel. One of the DMPS systems was used with a NanoDMA. The other was used with a LongDMA. For the calibration, three different particle mobility diameters were selected with a NanoDMA. After the selection, the monodisperse aerosol was measured by the two parallel DMPSs. The mobility diameter of 10 nm, 20 nm, and 30 nm was selected. As it turned out, the FWHM of the size distributions measured by the NanoDMPS and the LongDMPS are more similar at the mobility diameter 30 nm compared to the other measured mobility diameters. For that reason, the two PSD were combined at 30 nm. The time evolution of the PSD of the Vienna urban aerosol was measured during mid of January to the beginning of February. To compare the combined PSD measured by the DMPSs, a SMPS, placed next to the DMPSs, measured the PSD, during the same period. The mobility particle diameter of the PSD measured by the combined DMPS was in a mobility size range of 2.97 nm to 931.80 nm. The PSD measured by the SMPS system had a mobility particle diameter between 10.6 nm and 495.8 nm.

The results of this study indicate that the time evolution of the PSDs measured by the two parallel DMPSs can be combined very well at a mobility particle diameter of 30 nm. It can be seen that the structures of the PSD could be conserved. Comparing the time evaluations of the PSD measured by the SMPS and both DMPSs, it can be seen that the measured structures are very similar for each day. During that period, no $event$ could be identified. Nine $non\ events$ could be detected, and three days could be observed as $undefined$. One possible reason that no $event$ was measured is that the measurement took place during winter. Furthermore, it is interesting that not a weekly cycle of the total concentration could be observed, but a daily cycle could be identified. There were three significant peaks during most days. Only on Sunday, two peaks could be observed.

The results of this thesis fit very well in the existing literature. [22], [11] and [49], predicted that NPF events have a seasonal dependence. During winter, less NPF events could be expected compared to the rest of the year. This could be eventually the reason for the classification results. The current study was limited by time. For improved results, it is essential to measure during a more extended time period, preferably over one year, to have more precise classification results. Moreover, with long term measurements, the seasonal frequency could be proved with the used DMPSs. It is recommended to measure wind data during the measurement time because the

wind data could explain structures of the PSDs time evolution. Accessorily it is important to measure the ozone concentration during the measurement period due to the fact that the ozone concentration influences the new particle formation. Furthermore, the weekly and daily cycle can be determined more precisely with long term measurements.

Appendices

Appendix A

Acronyms

RF radiative forcing

ERF effective radiative forcing

ERFari effective radiative forcing from an aerosol-radiation interaction

ERFaci effective radiative forcing from an aerosol-cloud interaction

RHS right hand side

^{241}**Am** americium-241

DMA differential mobility analyser

CPC condensation particle counters

DMPS differential mobility particle sizer

NaCl Natriumchlorid

EMS electrical mobility spectrometer

FWHM full width at half maximum

PSD particle size distribution

AIM Aerosol Instrument Manager

SMPS scanning mobility particle sizer

NPF new particle formation

List of Figures

Bibliography

[1] William C Hinds. *Aerosol technology : properties, behavior, and measurement of airborne particles*. A Wiley-Interscience publication. Wiley, New York, NY [u.a.], 2. ed.. edition, 1999.

[2] John H Seinfeld. *Atmospheric chemistry and physics : from air pollution to climate change*. A Wiley-Interscience publication. Wiley, Hoboken, NJ, 2. ed.. edition, 2006.

[3] C. N Waters, J Zalasiewicz, C Summerhayes, A. D Barnosky, C Poirier, A Ga uszka, A Cearreta, M Edgeworth, E. C Ellis, M Ellis, C Jeandel, R Leinfelder, J. R McNeill, D. d Richter, W Steffen, J Syvitski, D Vidas, M Wagreich, M Williams, A Zhisheng, J Grinevald, E Odada, N Oreskes, and A. P Wolfe. The anthropocene is functionally and stratigraphically distinct from the holocene. *Science (American Association for the Advancement of Science)*, 351(6269):aad2622–aad2622, 2016.

[4] WHO. Health effects of particulate matter. policy implications for countries in eastern europe, caucasus and central asia. 2013. Copenhagen, Denmark.

[5] EEA. Air quality in europe — 2020 report. September 2020.

[6] J.-P Putaud, R Van Dingenen, A Alastuey, H Bauer, W Birmili, J Cyrys, H Flentje, S Fuzzi, R Gehrig, H.C Hansson, R.M Harrison, H Herrmann, R Hitzenberger, C Hüglin, A.M Jones, A Kasper-Giebl, G Kiss, A Kousa, T.A.J Kuhlbusch, G Löschau, W Maenhaut, A Molnar, T Moreno, J Pekkanen, C Perrino, M Pitz, H Puxbaum, X Querol, S Rodriguez, I Salma, J Schwarz, J Smolik, J Schneider, G Spindler, H ten Brink, J Tursic, M Viana, A Wiedensohler, and F Raes. A european aerosol phenomenology – 3: Physical and chemical characteristics of particulate matter from 60 rural, urban, and kerbside sites across europe. *Atmospheric environment (1994)*, 44(10):1308–1320, 2010.

[7] Günter Oberdörster ; Eva Oberdörster and Jan Oberdörster. Nanotoxicology: An emerging discipline evolving from studies of ultrafine particles. *Environmental health perspectives*, 113(7):823–839, 2005.

[8] Annette Peters, Bellina Veronesi, Lilian Calderón-Garcidueñas, Peter Gehr, Lung-Chi Chen, Marianne Geiser, William Reed, Barbara Rothen-Rutishauser, Samuel Schürch, and Holger Schulz. Translocation and potential neurological effects of fine and ultrafine particles a critical update. part fibre toxicol 3:13. *Particle and fibre toxicology*, 3:13, 02 2006.

[9] Boucher; O.D. Randall; P. Artaxo; C. Bretherton; G. Feingold; P. Forster; V.-M. Kerminen; Y. Kondo; H. Liao; U. Lohman; P. Rasch; S.K. Satheesh; S. Sherwood; B. Stevens;X.Y.

Zhang. 2013: Clouds and aerosols. in: Climate change 2013: The physical science basis. contribution of working group i to the fifth assessment report of the intergovernmental panel on climate change. *Cambridge University Press*, 2013. Cambridge, United Kingdom and New York, NY, USA.

[10] Stocker T.F., D. Qin, G.-K. Plattner, M. Tignor, S.K. Allen, J. Boschung, A. Nauels, Y. Xia, V. Bex, and P.M. Midgley (eds.). Ipcc, 2013: Summary for policymakers. in: Climate change 2013: The physical science basis. contribution of working group i to the fifth assessment report of the intergovernmental panel on climate change. *Cambridge University Press*. Cambridge, United Kingdom and New York, NY, USA.

[11] C Dameto de España, A Wonaschütz, G Steiner, B Rosati, A Demattio, H Schuh, and R Hitzenberger. Long-term quantitative field study of new particle formation (npf) events as a source of cloud condensation nuclei (ccn) in the urban background of vienna. *Atmospheric Environment*, 164:289–298, 2017.

[12] Peter W Atkins. *Physical chemistry*. Oxford Univ. Press, Oxford, 8. ed., 1. publ.. edition, 2006.

[13] Hanna Vehkamäki, Anni Määttänen, Antti Lauri, Markku Kulmala, Paul Winkler, Aron Vrtala, and Paul E Wagner. Heterogeneous multicomponent nucleation theorems for the analysis of nanoclusters. *The Journal of chemical physics*, 126(17):174707, 2007.

[14] N. H. Fletcher. Size Effect in Heterogeneous Nucleation. *The Journal of Chemical Physics*, 29(3):572–576, 1958.

[15] Markku Kulmala, Veli-Matti Kerminen, Tatu Anttila, Ari Laaksonen, and Colin D. O' Dowd. Organic aerosol formation via sulphate cluster activation. *Journal of Geophysical Research: Atmospheres*, 109(D4):n/a–n/a, 2004.

[16] Markku Kulmala, Liisa Pirjola, and Jyrki M. Mäkelä. Stable sulphate clusters as a source of new atmospheric particles. *Nature*, 404(6773):66, 2000.

[17] L. Ahlm, J. Julin, C. Fountoukis, S. N. Pandis, and I. Riipinen. Particle number concentrations over europe in 2030: the role of emissions and new particle formation. *Atmospheric Chemistry and Physics*, 13(20):10271, 2013.

[18] L. Skrabalova, N. Zikova, and V. Zdimal. Shrinkage of newly formed particles in an urban environment. *Aerosol and Air Quality Research*, 15(4):1313–1324, 2015.

[19] Markku Kulmala, Tuukka Petäjä, Tuomo Nieminen, Mikko Sipilä, Hanna E Manninen, Katrianne Lehtipalo, Miikka Dal Maso, Pasi P Aalto, Heikki Junninen, Pauli Paasonen, Ilona Riipinen, Kari E J Lehtinen, Ari Laaksonen, and Veli-Matti Kerminen. Measurement of the nucleation of atmospheric aerosol particles. *Nature Protocols*, 7(9):1651, 2012.

[20] W Birmili, H Berresheim, C Plass-Dulmer, T Elste, S Gilge, A Wiedensohler, and U Uhrner. The hohenpeissenberg aerosol formation experiment (hafex): a long-term study including

size-resolved aerosol, h2so4, oh, and monoterpenes measurements. *Atmospheric Chemistry And Physics*, 3:361–376, 2003.

[21] A Wiedensohler, N Ma, W Birmili, J Heintzenberg, F Ditas, M.O Andreae, and A Panov. Infrequent new particle formation over the remote boreal forest of siberia. *Atmospheric environment (1994)*, 200:167–169, 2019.

[22] Anna Wonaschütz, Anselm Demattio, Robert Wagner, Julia Burkart, Naděžda Zíková, Petr Vodička, Wolfgang Ludwig, Gerhard Steiner, Jaroslav Schwarz, and Regina Hitzenberger. Seasonality of new particle formation in vienna, austria – influence of air mass origin and aerosol chemical composition. *Atmospheric Environment*, 118:118–126, 2015.

[23] Tareq Hussein, Nahid Atashi, Larisa Sogacheva, Simo Hakala, Lubna Dada, Tuukka Petäjä, and Markku Kulmala. Characterization of urban new particle formation in amman—jordan. *Atmosphere*, 11(1):79, 2020.

[24] Astrid Kiendler-Scharr, Jürgen Wildt, Miikka Dal Maso, Thorsten Hohaus, Einhard Kleist, Thomas F Mentel, Ralf Tillmann, Ricarda Uerlings, Uli Schurr, and Andreas Wahner. New particle formation in forests inhibited by isoprene emissions. *Nature (London)*, 461(7262):381–384, 2009.

[25] N.S Holmes. A review of particle formation events and growth in the atmosphere in the various environments and discussion of mechanistic implications. *Atmospheric environment (1994)*, 41(10):2183–2201, 2007.

[26] Charles O Stanier, Andrey Y Khlystov, and Spyros N Pandis. Nucleation events during the pittsburgh air quality study: Description and relation to key meteorological, gas phase, and aerosol parameters special issue of aerosol science and technology on findings from the fine particulate matter supersites program. *Aerosol science and technology*, 38:253–264, 2004.

[27] M Kulmala, V.-M Kerminen, T Petäjä, A. J Ding, and L Wang. Atmospheric gas-to-particle conversion: why npf events are observed in megacities? *Faraday discussions*, 200:271–288, 2017.

[28] Mingyi Wang, Weimeng Kong, Ruby Marten, Xu-Cheng He, Dexian Chen, Joschka Pfeifer, Arto Heitto, Jenni Kontkanen, Lubna Dada, Andreas Kürten, Taina Yli-Juuti, Hanna E Manninen, Stavros Amanatidis, António Amorim, Rima Baalbaki, Andrea Baccarini, David M Bell, Barbara Bertozzi, Steffen Bräkling, Sophia Brilke, Lucía Caudillo Murillo, Randall Chiu, Biwu Chu, Louis-Philippe De Menezes, Jonathan Duplissy, Henning Finkenzeller, Loic Gonzalez Carracedo, Manuel Granzin, Roberto Guida, Armin Hansel, Victoria Hofbauer, Jordan Krechmer, Katrianne Lehtipalo, Houssni Lamkaddam, Markus Lampimäki, Chuan Ping Lee, Vladimir Makhmutov, Guillaume Marie, Serge Mathot, Roy L Mauldin, Bernhard Mentler, Tatjana Müller, Antti Onnela, Eva Partoll, Tuukka Petäjä, Maxim Philippov, Veronika Pospisilova, Ananth Ranjithkumar, Matti Rissanen, Birte Rörup, Wiebke Scholz, Jiali Shen, Mario Simon, Mikko Sipilä, Gerhard Steiner, Dominik Stolzenburg, Yee Jun Tham, António

Tomé, Andrea C Wagner, Dongyu S Wang, Yonghong Wang, Stefan K Weber, Paul M Winkler, Peter J Wlasits, Yusheng Wu, Mao Xiao, Qing Ye, Marcel Zauner-Wieczorek, Xueqin Zhou, Rainer Volkamer, Ilona Riipinen, Josef Dommen, Joachim Curtius, Urs Baltensperger, Markku Kulmala, Douglas R Worsnop, Jasper Kirkby, John H Seinfeld, Imad El-Haddad, Richard C Flagan, and Neil M Donahue. Rapid growth of new atmospheric particles by nitric acid and ammonia condensation. *Nature*, 581(7807):184–189, 2020.

[29] Tareq Hussein, Jyrki Martikainen, Heikki Junninen, Larisa Sogacheva, Robert Wagner, Miikka Dal Maso, Ilona Riipinen, Pasi P Aalto, and Markku Kulmala. Observation of regional new particle formation in the urban atmosphere. *Tellus B: Chemical and Physical Meteorology*, 60(4):509–521, 2008.

[30] J. Burkart, G. Steiner, G. Reischl, and R. Hitzenberger. Long-term study of cloud condensation nuclei (ccn) activation of the atmospheric aerosol in vienna. *Atmospheric Environment*, 45(33):5751, 2011.

[31] T Borsós, D Řimnáčová, V Ždímal, J Smolík, Z Wagner, T Weidinger, J Burkart, G Steiner, G Reischl, R Hitzenberger, J Schwarz, and I Salma. Comparison of particulate number concentrations in three central european capital cities. *The Science of the total environment*, 433:418–426, 2012.

[32] Gerhard Steiner and Georg P Reischl. The effect of carrier gas contaminants on the charging probability of aerosols under bipolar charging conditions. *Journal of Aerosol Science*, 54:21–31, 2012.

[33] Peter Kallinger, Gerhard Steiner, and Wladyslaw Szymanski. Characterization of four different bipolar charging devices for nanoparticle charge conditioning. *Journal of Nanoparticle Research*, 14(6):1–8, 2012.

[34] urlhttps://tsi.com/products/aerosol-neutralizers/advanced-aerosol-neutralizer-3088/.

[35] P. Kulkarni, P.A. Baron, and K. Willeke. *Aerosol Measurement: Principles, Techniques, and Applications: Third Edition*. John Wiley and Sons, 2011.

[36] G.P. Reischl. Measurement of ambient aerosols by the differential mobility analyzer method: Concepts and realization criteria for the size range between 2 and 500 nm. *Aerosol Science and Technology*, 14(1):5–24, 1991.

[37] W.Winklmayr; G.P.Reischl; A.O.Lindner; A.Berner. A new electromobility spectrometer for the measurement of aerosol size distributions in the size range from 1 to 1000 nm. *Aerosol Science and Technology*, 22(3):289–296, 1991.

[38] G Steiner, M Attoui, D Wimmer, and G. P Reischl. A medium flow, high-resolution vienna dma running in recirculating mode. *Aerosol Science and Technology*, 44(4):308–315, 2010.

[39] Peter Josef Wlasits. *On the effect of relative humidity on the activation of aerosol particles in butanol-based condensation particle counters*. Wien, 2019.

[40] *Model 3776 Ultrafine Condensation Particle CounterOperation and Service Manual*, April 2006.

[41] Mark R. Stolzenburg ; Peter H. McMurry. An ultrafine aerosol condensation nucleus counter. *Aerosol Science and Technology*, 14(1):48–65, 1991.

[42] https://tsi.com/products/aerosol-generators-dispersers/polydisperse-generators/aerosol-generator-3076/.

[43] A. Birmili, W. ;Wiedensohler. The design of a twin differential mobility particle sizer for a wide size range and great operation stability. *Journal of Aerosol Science*, 28(1):145–S146, 1997.

[44] *TSI SERIES 4000/4100HIGH PERFORMANCE LINEAR OEM MASS FLOWMETER (TSI MODELS 4021, 4024, 4121, AND 4122)*, February 2016.

[45] *EMS - 10 Control Center Operating Software EMSCC 1.4*.

[46] http://lindner-tac.at/home.html.

[47] *Aerosol InstrumentManager® Software for Condensation Particle Counters,EPCTM Environmental Particle CounterTM Monitor, Water-based Condensation Particle Counters, and Electrical Aerosol Detector*, October 2010.

[48] S. Pfeifer, W. Birmili, A. Schladitz, T. Müller, A. Nowak, and A. Wiedensohler. A fast and easy-to-implement inversion algorithm for mobility particle size spectrometers considering particle number size distribution information outside of the detection range. *Atmospheric Measurement Techniques*, 7(1):95–105, 2014.

[49] Tuomo Nieminen, Veli-Matti Kerminen, Tuukka Petäjä, Pasi P Aalto, Mikhail Arshinov, Eija Asmi, Urs Baltensperger, David C.S Beddows, Johan Paul Beukes, Don Collins, Aijun Ding, Roy M Harrison, Bas Henzing, Rakesh Hooda, Min Hu, Urmas Hõrrak, Niku Kivekäs, Kaupo Komsaare, Radovan Krejci, Adam Kristensson, Lauri Laakso, Ari Laaksonen, W Richard Leaitch, Heikki Lihavainen, Nikolaos Mihalopoulos, Zoltán Németh, Wei Nie, Colin O'Dowd, Imre Salma, Karine Sellegri, Birgitta Svenningsson, Erik Swietlicki, Peter Tunved, Vidmantas Ulevicius, Ville Vakkari, Marko Vana, Alfred Wiedensohler, Zhijun Wu, Annele Virtanen, and Markku Kulmala. Global analysis of continental boundary layer new particle formation based on long-term measurements. *Atmospheric chemistry and physics*, 18(19):14737–14756, 2018.